ACS APPLIED MATERIALS & INTERFACES

www.acsami.org

Research Article

Singlet Oxygen ($^1O_2$)-Mediated Tunable Photocatalytic H_2O_2 Generation Using Donor–Acceptor Conjugated Microporous Polymers

Atul Kapoor, Laraib Akhtar, Sanyam, Suman Karmakar, Anirban Mondal,* and Venkata Suresh Mothika*

Cite This: https://doi.org/10.1021/acsami.6c02471

Read Online

ACCESS | Metrics & More | Article Recommendations | Supporting Information

ABSTRACT: While generating hydrogen peroxide (H_2O_2) via a singlet oxygen ($^1O_2$) pathway is kinetically faster, it typically requires photocatalysts that exhibit efficient intersystem crossing (ISC). Herein, we report a series of donor–acceptor conjugated microporous polymers (CMPs), TPA-Btz, TPE-Btz, TPE-Ttz, and lpTPE-Btz, that produce H_2O_2 through the $^1O_2$ pathway without relying on ISC or triplet energy transfer, instead driven by efficient interfacial electron transfer. By systematic variation of the donor, and acceptor components of the CMP network, the exciton properties are finely tuned, revealing the structure–property relationship of CMPs and their photocatalytic performance. While all the CMPs have sufficiently high conduction band potentials to reduce oxygen into superoxide anions ($O_2^{\bullet-}$), *in situ* electron paramagnetic resonance (EPR) and scavenging studies revealed a significant contribution of the $^1O_2$ pathway for H_2O_2 formation. Among the CMPs, TPA-Btz showed remarkably high H_2O_2 production rates of 3.8 mmol g^{-1} h^{-1} in pure water, with an apparent quantum yield of 8.71% and a solar-to-chemical-conversion (SCC) efficiency of 2.6%. Comprehensive computational analysis confirmed that the oxygen reduction reaction (ORR) pathway is thermodynamically favorable in all the CMPs, with a higher ΔG value for TPA-Btz, corroborating experimental observations. We have also demonstrated the generation of gram-scale quantities of solid-form H_2O_2 ($Na_2CO_3{\cdot}1.5H_2O_2$), a step toward safer handling and transportation.

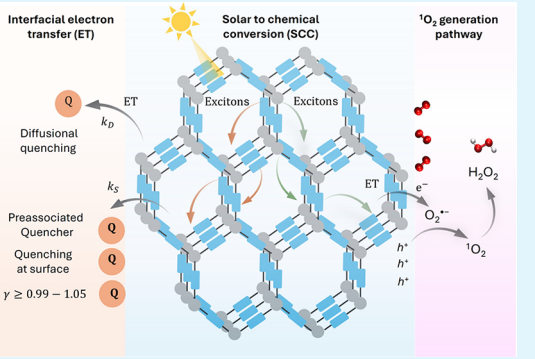

KEYWORDS: *photocatalysis, singlet oxygen, conjugated microporous polymers, H_2O_2 production, electron transfer, kinetics*

INTRODUCTION

Solar-driven hydrogen peroxide (H_2O_2) generation from water (H_2O) and oxygen (O_2) has emerged as a sustainable alternative approach to the energy-intensive and environmentally detrimental industrial anthraquinone oxidation process.[1,2] H_2O_2, as a clean fuel and oxidant, has applications in fuel cells, wastewater/industrial effluent treatment, etc.[3,4] Recently, π-conjugated microporous polymers (CMPs)[5−9] have emerged as promising photocatalysts for H_2O_2 generation due to their precise structural engineering, visible-light absorption, tunable optical band gaps, and efficient light-harvesting properties, as well as their ability to mimic the natural artificial photosynthesis process for photoredox reactions.[10−12] CMPs belong to the broader class of porous organic polymers (POPs) and consist of extended π-conjugated networks formed by the covalent linkage of aromatic units. The continuous π-conjugation imparts semiconducting characteristics, enabling efficient visible-light absorption and charge transport for photocatalytic processes. Importantly, the modular framework allows incorporation of donor–acceptor units and functional groups to tune optoelectronic properties, exciton dynamics, and catalytic activity. Moreover, their intrinsic porosity and network architecture facilitate mass transport and interfacial charge transfer, highlighting the critical role of structure–property relationships in conjugated polymer photocatalysts.[13]

CMPs reported so far for photocatalytic H_2O_2 generation undergo sequential two-step one-electron oxygen reduction (ORR) and follow the superoxide anion pathway ($O_2 \rightarrow O_2^{\bullet-} \rightarrow H_2O_2$).[14,15] Notably, the two-step one-electron ORR pathway possesses high energy barriers, may lead to side reactions, and reduces the selectivity of H_2O_2 formation.[16] Alternatively, the H_2O_2 synthesis through the $^1O_2$ pathway accelerates the kinetics of the ORR process and subsequent H_2O_2 yields.[17] However, the traditional method of producing $^1O_2$ involves photocatalysts that exhibit efficient intersystem crossing (ISC) and occurs via a triplet-state energy-transfer process. Recently, it has been reported that benzobisthiazole

Received: February 3, 2026
Revised: April 13, 2026
Accepted: April 19, 2026

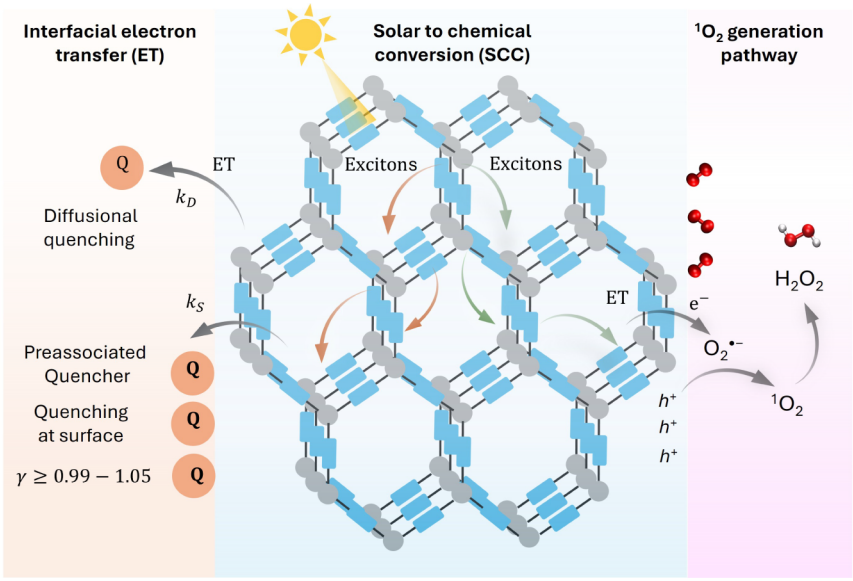

Figure 1. Schematic illustrating a nontraditional $^1O_2$-mediated photoredox pathway for H_2O_2 generation occurring via interfacial electron transfer (ET) (right). The approach employed for understanding interfacial ET kinetics using quencher Q is shown on left.

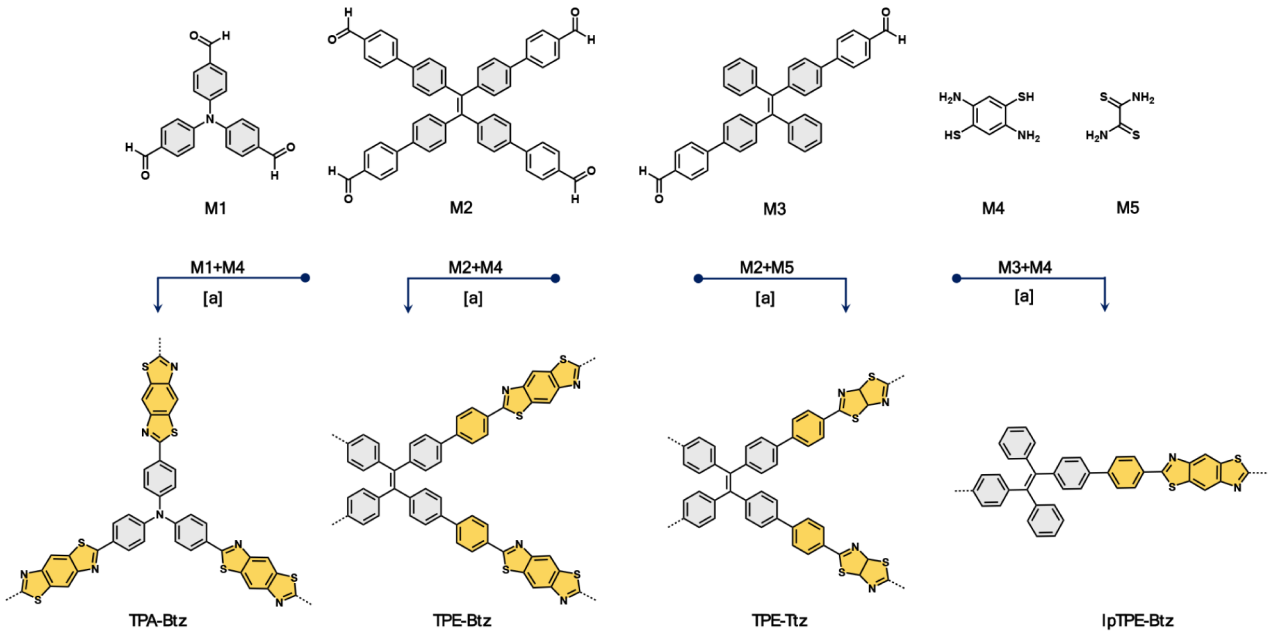

Figure 2. Synthetic pathway for donor−acceptor CMPs: depiction of molecular structures of monomers and chemical structures of elementary units of donor−acceptor CMPs, TPA-Btz, TPE-Btz, TPE-Ttz, and lpTPE-Btz CMPs. [a] Dimethylacetamide, 150 °C, 96 h.

linear conjugated polymers produce $^1O_2$ upon light irradiation of their aqueous dispersion via hole-induced oxidation of the *in situ*-generated superoxide anion ($O_2^{\bullet-}$).[18,19] Such a process significantly quenches holes and boosts interfacial electron-transfer rates, subsequently H_2O_2 yields.[20−22] This may be considered an autocatalytic cycle that produces continuous $^1O_2$ and accelerates the kinetics of H_2O_2 formation.[23,24] Moreover, computational machine learning (ML) approaches have recently emerged as powerful tools for predicting and high-throughput screening of organic photosensitizers for efficient singlet oxygen ($^1O_2$) generation. By enabling rapid exploration of vast chemical spaces and capturing nontrivial structure−property relationships, these methods have substantially accelerated the identification of promising candidates based on key photophysical descriptors. Recent studies have demonstrated the capability of ML-assisted frameworks to quantitatively correlate molecular features with $^1O_2$ quantum yields and guide the rational design of next-generation photosensitizers. Despite these advances, a detailed mechanistic understanding at the molecular level remains indispensable for elucidating the fundamental photophysical processes governing $^1O_2$ generation. In this context, the present work is specifically aimed at a comprehensive density functional theory (DFT)-based investigation to unravel the underlying excited-state pathways and mechanistic factors in selected systems. Such an approach provides complementary, physics-grounded insights that both support experimental

https://doi.org/10.1021/acsami.6c02471
ACS Appl. Mater. Interfaces XXXX, XXX, XXX−XXX

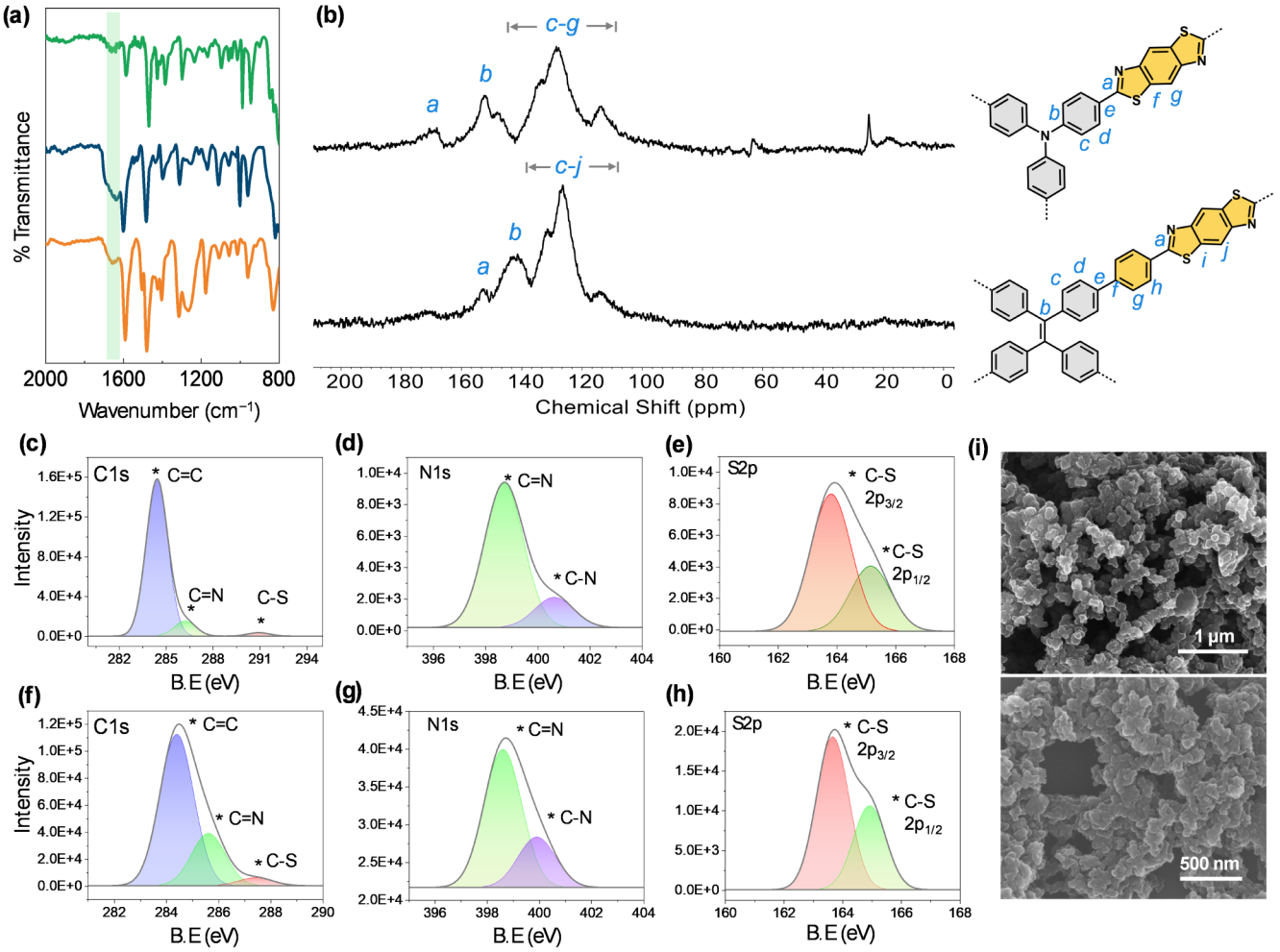

Figure 3. Structural characterization of CMPs: (a) FTIR spectra of TPA-Btz (orange), TPE-Btz (navy blue), and lpTPE-Btz (bright green); (b) solid-state $^{13}C-CP$ MAS NMR spectra of TPA-Btz and TPE-Btz. XPS analysis of TPA-Btz (c–e) and TPE-Btz (f–h), respectively, and (i) SEM images of TPA-Btz (above) and TPE-Btz (below).

observations and augment broader machine-learning-based screening strategies.[25−27]

Herein, we report a series of benzobisthiazole (Btz) and thiazolothiazole (Ttz) donor−acceptor CMPs, TPA-Btz, TPE-Btz, TPE-Ttz, and lpTPE-Btz, which produce H_2O_2 via $^1O_2$ without relying on ISC or triplet energy transfer. Instead, this process is driven by highly efficient photoinduced interfacial electron transfer (ET) and hole-induced oxidation of the *in situ*-generated $O_2^{\bullet-}$ (Figure 1).[28−31] All the CMPs exhibited excellent visible light absorption properties (up to 550 nm) due to intramolecular charge transfer (ICT) and showed optimum optical band gaps[11] of 2.38, 2.59, 2.41, and 2.56 eV, respectively, which are required for visible light photocatalysis.[32] The steady-state and time-resolved Stern−Volmer quenching analysis indicated that the fraction of excitons reaching the CMP/solution interface is nearly unity ($\gamma > 0.99$) in all the polymers. Additionally, the CMPs exhibit high direct ($k_S \approx 10^8$ s^{-1}) and diffusional ($k_D \approx 10^{11}$ M^{-1} s^{-1}) charge transfer rate constants. By systematically varying the donor and acceptor units, the exciton properties are precisely tuned, and among the CMPs, TPA-Btz exhibited superior photocatalytic H_2O_2 generation yields of up to 3.8 and 54.7 mmol g^{-1} h^{-1} in pure water and a 10% benzyl alcohol/H_2O mixture, respectively, due to its higher photocurrent response, longer excited-state lifetime (1.42 ns), lower exciton binding energy (70.91 meV), and higher contact potential difference (31.27 mV) compared to the linear polymer lpTPE-Btz. *In situ* EPR and scavenging experiments revealed the involvement of both $O_2^{\bullet-}$ and $^1O_2$ in the H_2O_2 formation. Further, comparative studies with the linear polymer lpTPE-Btz indicated that the three-dimensional network structure of CMPs is essential for achieving high H_2O_2 yields.[33]

The study provides systematic tuning of H_2O_2 photosynthesis through structural modulation, highlights interfacial charge-transfer kinetics—a crucial parameter in photoredox catalysis—and offers a nontraditional $^1O_2$-mediated photoredox pathway.

RESULTS AND DISCUSSION

Structural Characterization

The heterocyclic CMPs were synthesized by condensation of tri- or tetraformyl nodes with corresponding 2,5-diamino-1,4-benzenedithiol or dithiooxamide under high-temperature reaction conditions (Figure 2 and synthesis procedure in the SI). All of the polymers were thoroughly purified by Soxhlet

https://doi.org/10.1021/acsami.6c02471
ACS Appl. Mater. Interfaces XXXX, XXX, XXX−XXX

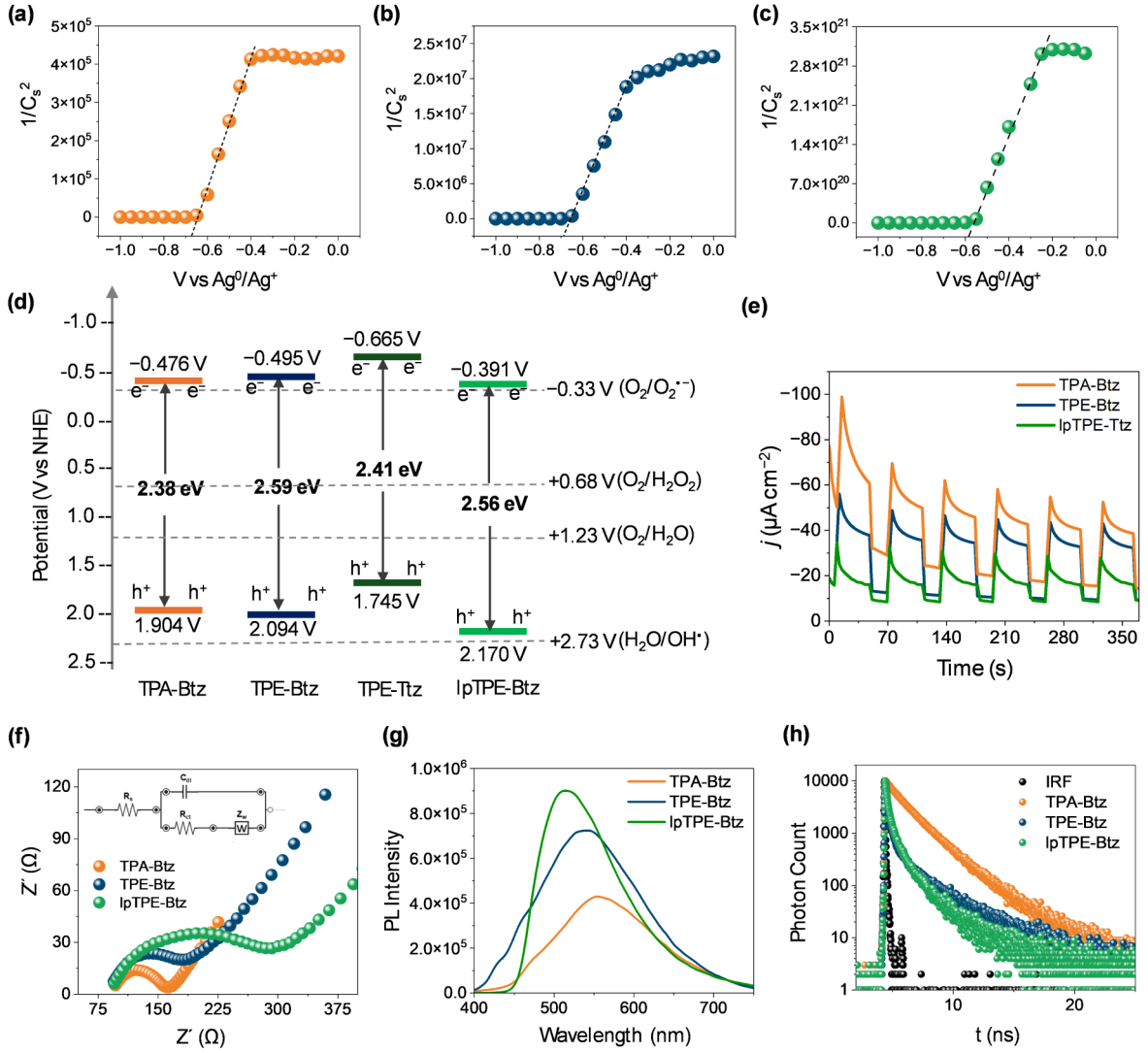

Figure 4. Donor−acceptor CMP photocatalyst properties: Mott−Schottky plots of (a) TPA-Btz, (b) TPE-Btz, and (c) lpTPE-Btz at the isoelectric point. (d) Representation of comparative electronic band structures of different CMPs; (e) photocurrent response profiles; (f) EIS measurements; (g) photoluminescence (PL) spectra in dispersed state; and (h) fluorescence excited state decay profiles of TPA-Btz, TPE-Btz, TPE-Ttz, and lpTPE-Btz.

extraction before use in further studies. The heterocyclic linkage formation was evident from the Fourier transform infrared spectroscopy (FTIR): as shown in Figure 3a, TPA-Btz showed characteristic −C═N ($\nu_{C=N}$) and −C−S (ν_{C-S}) stretching frequencies at 1662 and 828 cm^{-1}, respectively, confirming the formation of benzobis(thiazole) (Btz) linkage formation. Similar stretching bands were observed for TPE-Btz and lpTPE-Btz at 1636 and 820 cm^{-1} and 1673 and 814 cm^{-1}, respectively. As reported by us previously, the thiazolothiazole CMP, TPE-Ttz showed similar characteristic IR spectrum.[8] The absence of −C═O($\nu_{C=O}$) and −C−N (ν_{C-N}) stretching bands in the polymers indicates no residual monomers present in the corresponding polymers (Figures S1−S3). Further, the solid-state ^{13}C CP-MAS nuclear magnetic resonance (NMR) spectra showed signals at 169.37, 152.47 ppm and 152.91, 142.38 ppm, assigned to carbons of "S−C═N" and "C═C" of the Btz unit present in TPA-Btz and TPE-Btz, respectively (Figure 3b). Other aromatic carbons appeared in the range of 114 to 135 ppm for both polymers. These characteristic ^{13}C NMR signals confirmed the successful formation of the corresponding CMPs via heterocyclic linkages and are consistent with the literature.[34] X-ray photoelectron spectroscopy (XPS) confirmed the elemental composition and chemical environments of the CMPs, as shown in Figure 3c−h, the deconvoluted C 1s XPS spectrum of TPA-Btz showed peaks at 284.38, 285.62, and 287.46 eV, corresponding to the binding energy of C−C, C═C/C═N, and C−S, respectively. The N 1s spectrum showed peaks at 398.59, and 399.85 eV, corresponding to C═N and C−N, while the S 2p XPS showed doublets near 163.68 and 164.89 eV, corresponding to C−$S_2p_3/_2$, C−$S_2p_1/_2$. On the other hand, for TPE-Btz, the deconvoluted C 1s spectrum showed peaks at ∼284.38, 286.13, and 290.74 eV, corresponding to C−C, C═C/C═N, and C−S bonds, respectively.[35] The deconvoluted N 1s spectrum showed peaks at 398.69, and 400.63 eV, corresponding to C═N and C−N of the Btz moiety present in the CMPs. The deconvoluted S 2p XPS displayed peaks at 163.78 and 165.11 eV, assigned to C−$S_2p_3/_2$ and C−$S_2p_1/_2$ states. These binding energies are consistent with literature-reported Btz-based CMPs.[36,37]

https://doi.org/10.1021/acsami.6c02471
ACS Appl. Mater. Interfaces XXXX, XXX, XXX−XXX

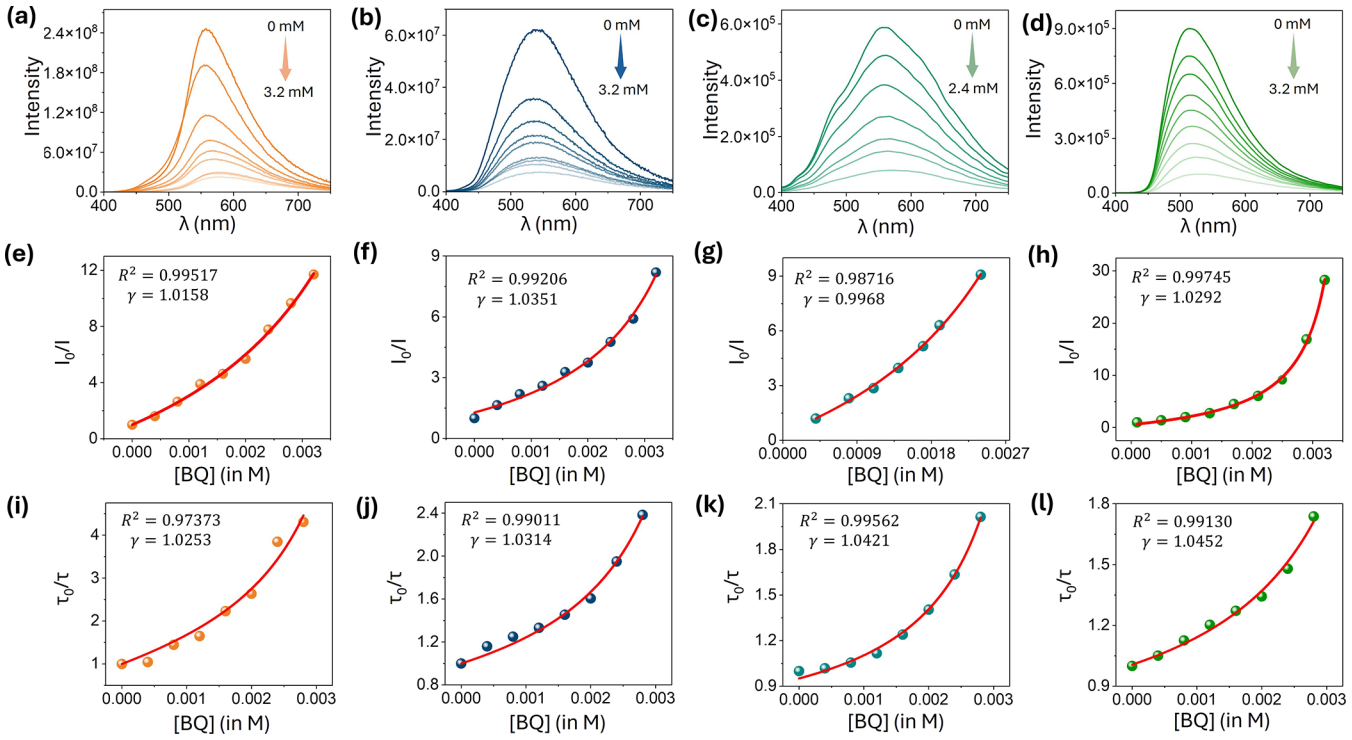

Figure 5. Steady-state and time-resolved Stern−Volmer analysis: fluorescence quenching of CMPs upon gradual addition of the quencher for (a) TPA-Btz, (b) TPE-Btz, (c) TPE-Ttz, and (d) lpTPE-Btz. Fluorescence intensity and excited state lifetime changes upon gradual addition of benzoquinone represented as I_0/I vs [BQ] and τ_0/τ vs [BQ], respectively, and their corresponding nonlinear fitting to eqs 1 and 2 for (e, i) TPA-Btz, (f, j) TPE-Btz, (g, k) TPE-Ttz, and (h, l) lpTPE-Btz. The fraction of excitons reaching the CMP surface (γ) after photoexcitation is shown in inset.

Thermogravimetric analysis (TGA) showed high thermal stability of the CMPs. For instance, TPA-Btz and TPE-Btz showed only 5.8% weight loss up to 555 and 552 °C, indicating high thermal stability of the CMPs due to their network structure. A significant weight loss (ca. 63%) was observed upon further heating to 800 °C for both CMPs (Figure S4). The nitrogen (N_2) adsorption isotherms measured at 77 K revealed type-II profiles for both TPA-Btz and TPE-Btz, with a total uptake of 51 and 63 mL g^{-1} and Brunauer−Emmett−Teller (BET) surface areas of 63.74 and 85.2 m^2 g^{-1}, respectively (Figure S5). Additionally, the average pore size was found to be ca. 1.24 nm, obtained via the NL-DFT method for both TPA-Btz and TPE-Btz. These results suggest a porous network structure with extended π-conjugation and small molecule-accessible micropores, which will impact the heterogeneous photocatalytic outcome compared to non-porous linear π-conjugated polymers (*vide infra*). As expected, all the CMPs displayed only broad peaks in the powder X-ray diffraction (PXRD) patterns in the range of 5°−35°, suggesting the amorphous nature of the CMPs (Figure S6). Field-emission scanning electron microscopy (FESEM) images of both TPA-Btz and TPE-Btz revealed fused irregular particles of submicrometer size, and elemental mapping by energy-dispersive X-ray spectroscopy (EDS) confirmed the uniform distribution of C, N, and S in the CMPs (Figures 3i and S7−S10). Transmission electron microscopy (TEM) also displayed similar irregular particle assemblies at lower magnifications; however, upon further magnification, it revealed ensembles of CMP layer-like structures that are typically observed for CMPs (Figure S11).[38,39]

Visible Light Absorption and Band Potentials

Measured by diffuse reflectance spectroscopy (DRS), all the CMPs, including lpTPE-Btz, showed broad solid-state absorption spectra extending up to 550 nm, with calculated optical band gaps (ΔE_g) of 2.38, 2.59, 2.41, and 2.56 eV for TPA-Btz, TPE-Btz, TPE-Ttz, and lpTPE-Btz, respectively (Figure S12). The increased band gap of the linear polymer lpTPE-Btz is a consequence of the decreased degree of π-conjugation compared to the π-conjugated networks of CMPs. Notably, such an optical band gap range of CMPs has been reported to be optimal for efficient photocatalytic reactions, such as photocatalytic H_2 evolution, oxygen reduction reaction (ORR), CO_2 reduction, or even H_2O_2 generation applications.[17,40] Simultaneously, Mott−Schottky analyses were performed to understand the conduction band potentials of CMPs, as shown in Figure 4a−c, and the reciprocal of the square of capacitance ($1/C^2$) vs applied potential resulted in a Mott−Schottky plot with a positive slope for all the CMPs, indicating their *n*-type semiconductor characteristics. The conduction band potentials (CB) were found to be −0.476, −0.495, −0.665, and −0.391 eV vs NHE (pH ≈ 7) for TPA-Btz, TPE-Btz, TPE-Ttz, and lpTPE-Btz, respectively. These CB potentials of CMPs are more negative than the indirect and direct $2e^-$ oxygen reduction potentials, i.e., O_2 to superoxide radicals, $O_2^{\bullet^-}$ ($E^0_{O2/O2\cdot-}$= − 0.33 V vs NHE) and ($E^0_{O2/H2O2}$= 0.68 V vs NHE), suggesting possible H_2O_2 generation via oxygen reduction reactions (Figure 4d). The valence band potentials (VB) were determined by combining the optical band gaps with CB using the equation $E_g = E_{VB} - E_{CB}$ and were found to be 1.904, 2.094, 1.745, and 2.170 eV vs NHE (pH ≈ 7) for TPA-Btz, TPE-Btz, TPE-Ttz, and lpTPE-Btz,

https://doi.org/10.1021/acsami.6c02471
ACS Appl. Mater. Interfaces XXXX, XXX, XXX−XXX

Table 1. Fitting Parameters Deduced from the Steady-State Stern–Volmer Analysis of I_0/I vs [BQ] Obtained from eq 1

CMP	PL QY (%)	K_A (M^{-1})	γ	k_S ($\times 10^8$ s^{-1})	k_D ($\times 10^{11}$ M^{-1} s^{-1})
TPA-Btz	12.066	30.9 ± 0.1575	1.01	4.419 ± 2.6443	17.12 ± 0.4415
TPE-Btz	8.662	56.7 ± 0.0728	1.03	33.86 ± 0.6830	22.67 ± 0.7959
TPE-Ttz	5.051	85.45 ± 0.0821	0.9968	18.314 ± 1.7090	61.45 ± 0.1558
lpTPE-Btz	3.243	109.2 ± 0.0648	1.02	45.921 ± 0.2234	12.65 ± 0.0604

respectively. The VB potentials are more negative than the water oxidation potentials ($E^0_{H2O/O2}$= 1.23 V vs NHE) and ($E^0_{H2O/H2O2}$ = 2.73 V vs NHE), indicating possible water oxidation pathways for H_2O_2 generation. As seen in Figure 4e of transient photocurrent curves, TPA-Btz showed the highest photocurrent density, while lpTPE-Btz showed the lowest. In contrast, electrochemical impedance spectroscopy (EIS) performed on CMP-modified ITO electrodes in 0.1 M PBS in the frequency range of 100 kHz to 0.1 Hz resulted in a Nyquist plot with a small semicircle and lower charge transfer resistance (R_{ct}) of 66.66 and 89.23 Ω cm² for TPA-Btz and TPE-Btz, respectively (Figure 4f). On the other hand, lpTPE-Btz showed a larger semicircle with an R_{ct} of 196.49 Ω cm^2. These results, together with photocurrent measurements, suggest higher charge-carrier generation and lower interfacial charge-transfer resistance for TPA-Btz among all the CMPs, indicating its possible superior photocatalytic properties. In line with this, the lower emission intensities and longer excited-state lifetimes of TPA-Btz (1.42 ns) and TPE-Btz (0.29 ns) compared to lpTPE-Btz (0.19 ns) indicated longer exciton migration and slower charge-carrier recombination (Figure 4g,h). These properties are essential for efficient solar-to-chemical energy conversion and for driving chemical reactions by a photocatalyst.

Interfacial Electron Transfer and Charge Carrier Separation

In the case of π-conjugated microporous polymers, upon light absorption, the exciton generated migrates to the CMP surface and undergoes charge separation into free charge carriers, which perform targeted photoredox reactions at the CMP surface.[32,41] It is reported that π-conjugated microporous polymers (CMPs) exhibit efficient light-harvesting properties with high energy transfer efficiency, demonstrating efficient photoinduced interfacial electron transfer to small molecule quenchers at the CMP/solution interface.[42] Additionally, it was demonstrated that the fluorescence quenching efficiency of π-conjugated microporous polymers is relatively higher than that of linear polymers due to efficient exciton migration over a 3D CMP network and the micropore confinement of the quencher. In order to demonstrate the efficient exciton migration and electron transfer in the donor–acceptor CMPs under study, the Stern–Volmer fluorescence quenching analysis was conducted with the benzoquinone (BQ) quencher.[43,44] The exciton migration and interfacial electron transfer properties were demonstrated by steady-state and time-resolved fluorescence quenching measurements.[45] As seen in Figure 5a–d, the fluorescence of TPA-Btz, TPE-Btz, and lpTPE-Btz was significantly quenched (up to 92%) with the gradual addition of BQ (0–3 mM), indicating the efficient exciton migration properties of the CMPs. This quenching was further supported by time-resolved photoluminescence studies, where the average lifetime decreased markedly upon the addition of BQ, confirming a dynamic quenching mechanism and rapid exciton transfer within the polymer networks (Figure S13). The Stern–Volmer plot I_0/I vs [BQ]) showed linear behavior at the low quencher concentration regime (Figures S16,S17); however, it showed a positively deviated nonlinear curve at high concentrations (Figure 5e–h). The time-resolved Stern–Volmer plot (τ_0/τ vs [BQ]) also revealed such nonlinear changes at high concentrations, indicating a combination of static and dynamic quenching pathways at high concentrations (Figure 5i–l). Interestingly, TPA-Btz and TPE-Btz showed relatively higher deviations compared to lpTPE-Btz, and the fluorescence quenching was higher in the linear polymer, indicating faster radiative recombination compared to CMPs, potentially due to the rigid CMP framework-assisted enhanced exciton migration. This may result in higher charge-carrier separation and better surface charge generation for improved photocatalytic chemical conversion (*vide infra*). The linear response of I_0/I vs [BQ] or τ_0/τ vs [BQ] at lower concentrations suggests fluorescence quenching via preassociation of the BQ quencher with CMP, while the nonlinear response at high concentrations suggests a combination of static and dynamic quenching pathways.[42,46] Here, static quenching was assumed to be the dominant quenching mechanism at low concentrations, where the host–guest interactions (π-π stacking) between the electron-rich aromatic polymer network and benzoquinone result in ground-state complexation. It is known that conjugated microporous polymers exhibit an amplified quenching response even to trace analytes (in solution or vapor phase) due to efficient host–guest interactions within the confined nanopores.[12] The high quenching efficiency and quick response time are due to preassociated complex formation rather than slow collisional quenching (the dynamic pathway), which is limited by analyte diffusion into the pores and kinetic barriers. The low concentration (0–100 μM) static quenching Stern–Volmer constant (K_{SV}) was found to be 1.592 × 10^4 M^{-1}, 3.485 × 10^4 M^{-1}, 2.628 × 10^4 M^{-1}, and 2.134 × 10^4 M^{-1} for TPA-Btz, TPE-Btz, TPE-Ttz, and lpTPE-Btz, respectively (Figures S14–S17).

Upon excitation of the CMP, the excitons migrate from the interior bulk of the CMP to the surface/interface, where either direct or diffusional charge transfer to the quencher occurs, i.e., either static or diffusional quenching, or both, and it can be represented by eqs 1 and 2,

$$\frac{I_0}{I} = \left[(1-\gamma) + \gamma F_{SQ}\frac{k_{CMP*}}{k_{CMP*}+k_S} + \gamma(1-F_{SQ})\frac{k_{CMP*}}{k_{CMP*}+k_D[Q]}\right]^{-1} \quad (1)$$

$$\frac{\tau_0}{\tau} = \frac{1}{k_{CMP}*<\tau>} \quad (2)$$

Here, γ represents the fraction of excitons reached CMP/solution interface, $1-\gamma$ denotes the fraction of excited states confined within the inner regions that are inaccessible to the

https://doi.org/10.1021/acsami.6c02471
ACS Appl. Mater. Interfaces XXXX, XXX, XXX–XXX

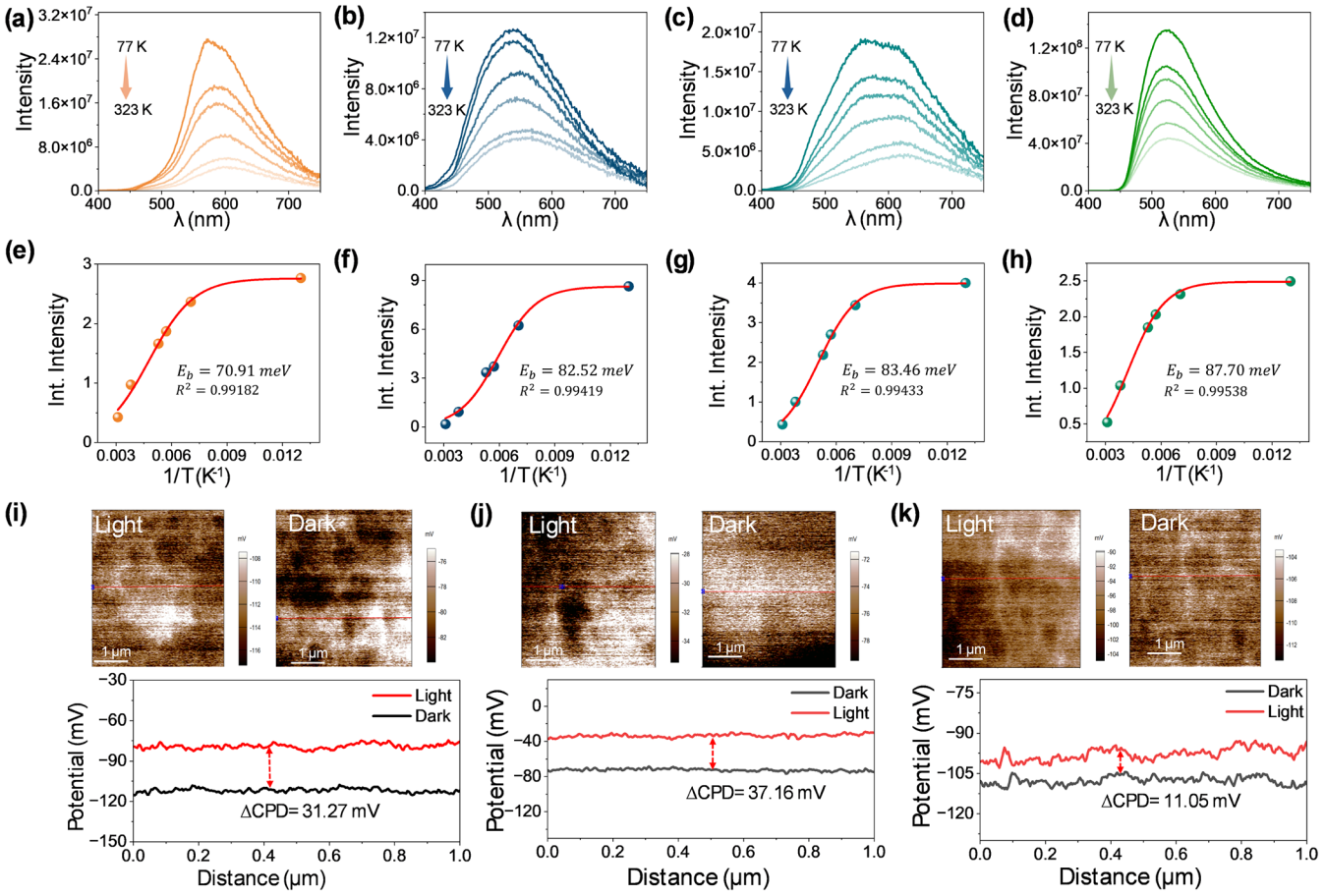

Figure 6. Exciton binding energies and surface potentials: Temperature-dependent fluorescence of (a) TPA-Btz, (b) TPE-Btz, (c) TPE-Ttz, (d) lpTPE-Btz, and (e–h) corresponding integrated PL intensity versus inverse temperature ($1/T$ fitted to the Arrhenius equation (eq 4)). The E_b values are given within the plot. KPFM images of CMPs under light and dark conditions (top) and corresponding surface potential difference plots for (i) TPA-Btz, (j) TPE-Btz, and (k) TPE-Ttz, respectively.

quencher, k_{CMP*} corresponds to the rate of excited state decay of CMP in the absence of the quencher and equals $1/\tau_0$, F_{SQ} represents the fraction of quencher-adsorbed sites, k_S is the rate constant of quenching at the surface, and k_D is the diffusional quenching rate constant at the CMP/solution interface.

The nonlinear curve of I_0/I vs [BQ] or τ_0/τ vs [BQ] fits well with eqs 1 and 2 and further analysis using eqs S1–S14 provides the parameters of γ, K_A, k_D, and k_S (Table 1). In all cases, the γ value reached near unity (>0.999), indicating efficient exciton migration from the interior of CMP to the surface, and the high k_S and k_D values indicate faster interfacial direct or diffusional electron transfer. The fluorescence quenching was also fitted to the Lehrer eq 3[47] (eqs S15, S16) to calculate the diffusional quenching rate constant (Figures S18,S19) and it aligns with the above calculations,

$$\frac{F_0}{F_0 - F} = \frac{F_0}{\Delta F} = \frac{1}{\alpha} + \frac{1}{\alpha K_{SV}[Q]} \quad (3)$$

Where F_0 is the PL intensity of CMP without quencher, ΔF represents the change in the fluorescence upon the addition of the quencher, α represents the fraction of excitons that reach the CMP/solution interface, and $k_D = \alpha K_{SV}$.

These results suggest that the light-induced excitons of all the CMPs readily migrate to the CMP surface and exhibit efficient interfacial electron transfer kinetics to drive the chemical conversions at the interface.[48] To understand the exciton binding energy (E_b) value, a key parameter reflecting the Coulombic interaction between photogenerated e^- and h^+,[49] temperature-dependent photoluminescence (PL) measurements were performed. As shown in Figure 6a–d, the fluorescence intensity of all the polymers increased with a decrease in temperature, and fitting the integrated PL intensities of CMPs to the Arrhenius equation (eq 4) resulted in corresponding E_b values of 70.91, 82.52, 83.46, and 87.70 meV for TPA-Btz, TPE-Btz, TPE-Ttz, and lpTPE-Btz, respectively (Figure 6e–h).

$$I(T) = \frac{I_0}{1 + A\exp\left(-\frac{E_b}{k_B T}\right)} \quad (4)$$

Where I_0 is the PL intensity at 77 K, T is the temperature in K, k_B is the Boltzmann constant, and A is a fitting parameter. The results indicate that TPA-Btz possesses the lowest E_b, while lpTPE-Btz exhibits the highest. A smaller E_b corresponds to weaker Coulombic attraction between e^-–h^+ pairs, facilitating easier exciton dissociation into free charge carriers.[50] Therefore, excitons in TPA-Btz can exhibit a lower exciton recombination rate and separate into long-lived free charge carriers better than other CMPs.[51] In contrast, the larger E_b observed for lpTPE-Btz implies relatively stronger exciton binding, leading to a higher probability of radiative

https://doi.org/10.1021/acsami.6c02471
ACS Appl. Mater. Interfaces XXXX, XXX, XXX–XXX

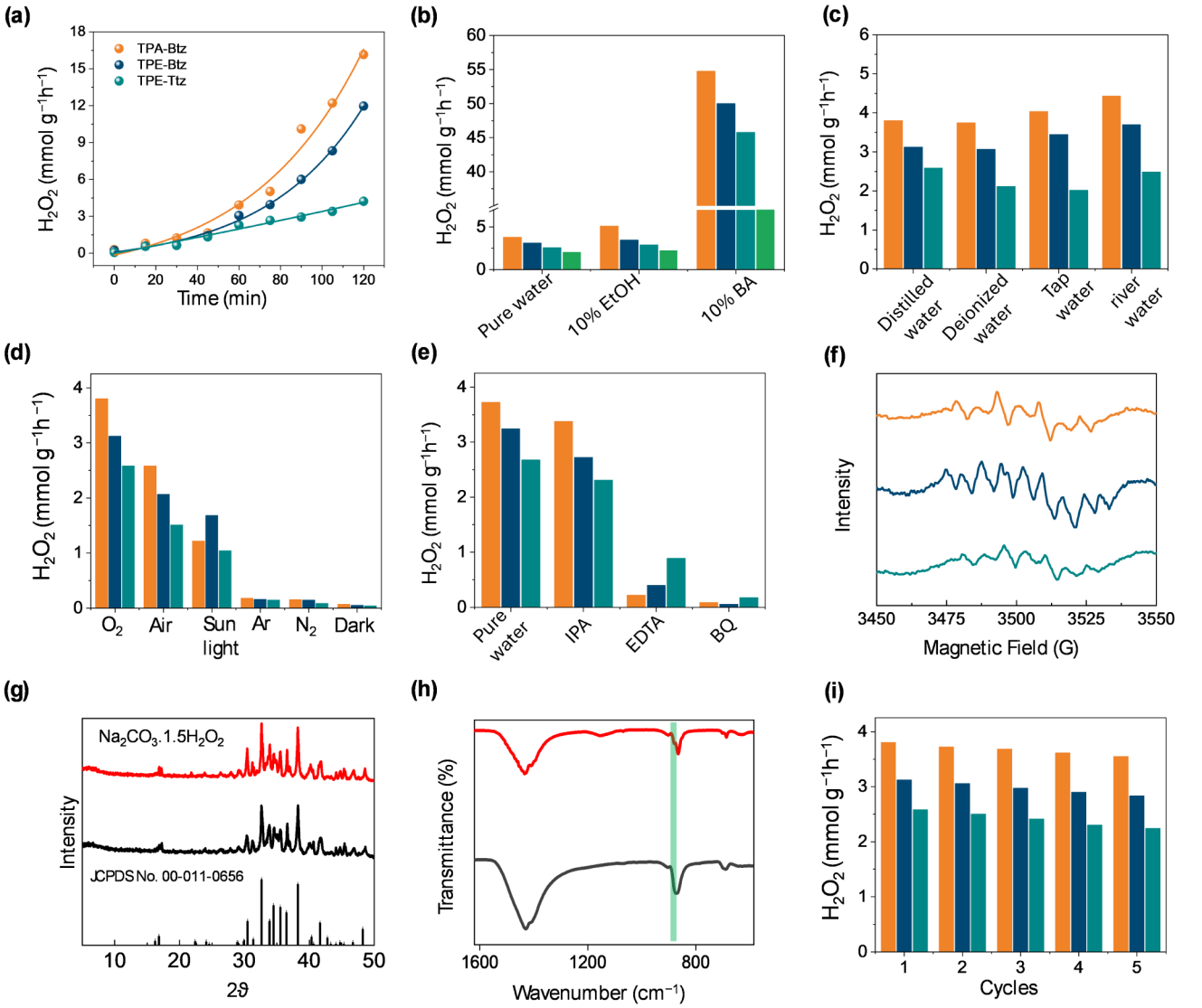

Figure 7. Photocatalytic H_2O_2 generation analysis: (a) Time-dependent photocatalytic H_2O_2 generation of TPA-Btz (orange), TPE-Btz (navy blue), and TPE-Ttz (light green); (b) H_2O_2 yields of CMPs in the presence of different sacrificial electron donors; (c) H_2O_2 yields of different CMPs with different water sources; (d) H_2O_2 yields for different CMPs in pure water saturated with O_2, Air, Ar, N_2, and under sunlight and dark conditions; (e) changes in the H_2O_2 generation rates for different CMPs upon the addition of reactive oxygen species scavengers; and (f) EPR spectra of DMPO-adduct produced *in situ* during photocatalysis. In all cases above, TPA-Btz, TPE-Btz, TPE-Ttz, and lpTPE-Btz are represented in orange, navy blue, light green, and bright green, respectively. (g) Comparison of PXRD of $Na_2CO_3{\cdot}1.5H_2O_2$ formed from commercial H_2O_2 (black), photocatalytically produced H_2O_2 (red), with H_2O_2 stick pattern (black). (h) FT-IR spectra of Na_2CO_3 (black) and $Na_2CO_3{\cdot}1.5H_2O_2$ (red). (i) Recyclability analysis: changes in H_2O_2 yields for CMPs over five cycles.

recombination (also evident in Stern−Volmer analysis) and comparatively reduced charge separation efficiency.[6] These results are further substantiated by light-induced surface charge potentials measured by Kelvin probe force microscopy (KPFM) under light and dark conditions. As depicted in Figures 6i−k and S20, the contact potential difference (ΔCPD) was found to be higher for TPA-Btz (31.27 mV) and TPE-Btz (37.16 mV) compared to TPE-Ttz (11.05 mV) and lpTPE-Btz (4.29 mV), indicating enhanced photoinduced charge redistribution on TPA-Btz and TPE-Btz. Further, from the built-in electric field (E) equation, $E = \Delta V/d$, where ΔV represents the contact potential difference obtained from the KPFM line profile and d denotes the corresponding spatial distance,[52] it can be visualized that TPA-Btz and TPE-Btz exhibit a stronger built-in electric field and facilitate efficient charge separation and directional charge transport under light irradiation.[53] The above results indicate that while all the CMPs exhibit excellent energy transfer and electron transfer, TPA-Btz has a lower excitonic binding energy, shows high light-induced surface charges, a higher photocurrent response, and can demonstrate relatively improved photocatalytic H_2O_2 generation efficiency compared to other polymers.

Photocatalytic H_2O_2 Generation

The photocatalytic performance was evaluated by varying the CMP catalyst dosage and pH of the reaction medium. A catalyst dosage of 5 mg was optimal, and pH 7 showed the highest H_2O_2 generation (Figure S21). At low pH, these heteroatom-containing CMPs can be protonated, thereby increasing surface charge, hindering effective O_2 adsorption on the photocatalyst surface, and consequently reducing the oxygen reduction reaction. On the other hand, at higher pH,

https://doi.org/10.1021/acsami.6c02471
ACS Appl. Mater. Interfaces XXXX, XXX, XXX−XXX

the limited proton availability for protonating superoxide anion suppresses H_2O_2 production. Also, H_2O_2 decomposes at a high pH, leading to low yields. Thus, pH 7 is optimal for H_2O_2 production.[54] Further, the effect of reaction temperature was investigated by performing photocatalytic H_2O_2 generation in the temperature range of 20−60 °C. As shown in Figure S22, the H_2O_2 production rate gradually decreased with increasing temperature for TPA-Btz, TPE-Btz, and TPE-Ttz photocatalysts. This may be due to the reduced solubility of dissolved O_2 at higher temperatures and also to thermal decomposition of generated H_2O_2. Thus, room temperature is optimal for photocatalytic H_2O_2 generation. The apparent quantum yield (AQY) of CMPs measured at 390 nm was found to be 8.71%, 6.71%, 5.43% and at 456 nm was found to be 7.40%, 5.28%, and 4.64% for TPA-Btz, TPE-Btz and TPE-Ttz, respectively (Figure S23), which were calculated using eqs S17,S18. This corresponds to a solar to chemical conversion (SCC) efficiencies of 2.6%, 2.16%, and 1.40% for TPA-Btz, TPE-Btz, and TPE-Ttz, respectively (eq S19). The relatively higher SCC values of TPA-Btz suggest its better photocatalytic efficiency and SCC conversion capabilities. The photocatalytic H_2O_2 generation performance of TPA-Btz, TPE-Btz, TPE-Ttz, and lpTPE-Btz was investigated using water resources such as river water, tap water, distilled water, and deionized water by dispersing 5 mg of CMP catalyst and specified light irradiation time under 300W Xe lamp or direct sunlight conditions. As shown in Figure 7a, TPA-Btz showed the highest photocatalytic H_2O_2 generation rate of 3.8 mmol g^{-1} h^{-1} followed by TPE-Btz (3.1 mmol g^{-1} h^{-1}), TPE-Ttz (2.5 mmol g^{-1} h^{-1}), and lpTPE-Btz (2.0 mmol g^{-1} h^{-1}) in distilled water. These values are relatively higher than other CMPs and comparable with COFs reported in the literature (Table S1).[55−57] Notably, the concentration of H_2O_2 gradually increased with the irradiation time and continued to increase up to 5 h in distilled water, indicating sustained photocatalytic activity and good stability of the catalysts under prolonged illumination (Figure S24). Furthermore, TPA-Btz outperforms TPE-Btz in photocatalytic H_2O_2 generation, despite having a lower surface area because TPA-Btz have higher intramolecular charge transfer efficiency, better photocurrent response, low recombination rates, conduction band potentials and longer excited state lifetimes, also play a critical role in photocatalytic H_2O_2 generation output.[58,59] Interestingly, the photocatalytic H_2O_2 generation was dramatically increased when added with a sacrificial donor such as benzyl alcohol (BA), for instance, the H_2O_2 production value increased from 3.8 to 54.7 mmol g^{-1} h^{-1} (a 14-fold increase) with TPA-Btz photocatalyst when a 10% benzyl alcohol: water (1:9 BA:H_2O) mixture was used. Similar enhancements were observed with other CMPs; for instance, TPE-Btz, TPE-Ttz, and lpTPE-Btz showed 50.01, 45.7, and 26.4 mmol g^{-1} h^{-1} (Figure 7b). As alluded to in the previous reports using COFs, such dramatic enhancement of H_2O_2 production could be attributed to the biphasic reaction medium (BA-H_2O) where the photoactive CMP catalyst remains dispersed in the organic phase, while the CMP produced H_2O_2 enters the aqueous phase immediately, avoiding the CMP-catalyst driven decomposition.[60,61] Albeit moderate increments of H_2O_2 production were observed when the photocatalytic reaction was performed in a 10% ethanol: water mixture (1:9 EtOH:H_2O), for instance, TPA-Btz, TPE-Btz, TPE-Ttz, and lpTPE-Btz produced 5.1, 3.4, 2.8, and 2.2 mmol g^{-1} h^{-1} of H_2O_2 as calculated by iodometric titration (Figures 7b, S25). Photocatalytic H_2O_2 production rates were also calculated using different water resources. Interestingly, the H_2O_2 production rates were found to be higher for river water (4.43, 3.69, 2.48 mmol g^{-1} h^{-1} for TPA-Btz, TPE-Btz, TPE-Ttz, respectively) compared to tap water (4.0, 3.4, 2.0 mmol g^{-1} h^{-1} for TPA-Btz, TPE-Btz, TPE-Ttz, respectively) and deionized water (3.7, 3.0, 2.1 mmol g^{-1} h^{-1} for TPA-Btz, TPE-Btz, TPE-Ttz, respectively) (Figure 7c). These results demonstrate the direct generation of H_2O_2 using natural water resources and thus significantly reduce the cost of H_2O_2 production using the CMPs under study. Subsequently, the role of light energy and an O_2-rich reaction medium was evaluated: as shown in Figure 7d, H_2O_2 production rate significantly reduced under dark, argon (Ar), and nitrogen (N_2) bubbled solution conditions, indicating the importance of light energy and the presence of O_2 for the successful photocatalytic generation of H_2O_2. Interestingly, the H_2O_2 production experiments performed under an air balloon provided H_2O_2 generation of up to 2.5, 2.0, and 1.5 mmol g^{-1} h^{-1} for TPA-Btz, TPE-Btz, and TPE-Ttz, respectively. To realize the practical utility of the CMPs, the H_2O_2 generation experiments were also performed under direct sunlight, as shown in Figure 7d, and CMPs showed moderate H_2O_2 production rates of 1.2, 1.6, and 1.0 mmol g^{-1} h^{-1} for TPA-Btz, TPE-Btz, and TPE-Ttz, respectively. The photogenerated H_2O_2 can decompose to H_2O or O_2 upon interaction with photogenerated electrons (e^-) or holes (h^+) present at the CMP catalyst surface.

To understand the dynamics of H_2O_2 formation and decomposition, kinetic analysis was performed. The rate of H_2O_2 formation follows zero-order kinetics and is independent of its concentration. On the other hand, the rate of H_2O_2 decomposition is directly proportional to its concentration, adhering to first-order kinetics.[60,62] Considering constant H_2O_2 formation and its simultaneous decomposition, the net H_2O_2 produced can be described using eq 5,

$$[H_2O_2] = \frac{k_f}{k_d} \times \{1 - \exp(-k_d \times t)\} \quad (5)$$

Where $[H_2O_2]$ describes the net concentration of photogenerated H_2O_2, t reaction time, k_f and k_d represent the rate constants of H_2O_2 formation and decomposition, respectively.

Linear fitting of $[H_2O_2]$ formed vs t resulted in k_f values of 3.936×10^3, 2.9×10^3, and 2.2×10^3 μM h^{-1}, for TPA-Btz, TPE-Btz, and TPE-Ttz, respectively. On the other hand, the k_d values were found to be 1.6×10^{-2}, 1.9×10^{-2}, and 2.2×10^{-2} h^{-1}, respectively. These results suggest that the photolytic decomposition of H_2O_2 in the presence of the CMP catalyst is relatively slow. These findings are further substantiated through photocatalytic decomposition measurements of a known H_2O_2 solution in the presence of CMP under N_2 atmospheric conditions (Figures S26−S29). The H_2O_2 decomposition was examined in a biphasic medium (10% BA/H_2O). As shown in Figure S30, the k_d values in the biphasic medium were found to be 0.385, 0.340, and 0.237 h^{-1} for TPA-Btz, TPE-Btz, and TPE-Ttz, respectively, which are relatively higher compared to monophasic (H_2O) systems. The corresponding k_f values were found to be 5.706×10^4, 4.173×10^4, and 2.706×10^4 μM h^{-1} (Figure S31 and Table S2). However, the ratio k_f/k_d for the biphasic system is relatively lower than that of the monophasic system, suggesting a higher net H_2O_2 yield in the biphasic system. The photogenerated H_2O_2 enabled *in situ* degradation of organic pollutants, such as

https://doi.org/10.1021/acsami.6c02471
ACS Appl. Mater. Interfaces XXXX, XXX, XXX−XXX

Rhodamine B (RhB), with over 85% dye degradation efficiency within 60 min (Figure S32).

Mechanistic Understanding of H_2O_2 Formation

To understand the mechanistic pathway of photocatalytic H_2O_2 formation, initially, scavenging studies were performed to understand the major reactive oxygen species involved in forming desired H_2O_2. Upon introduction of 10 mM *p*-benzoquinone (*p*-BQ) ($O_2^{\bullet-}$ scavenger), the H_2O_2 production rate has dropped from 3.8 to 0.086 mmol g^{-1} h^{-1} for TPA-Btz, 3.4 to 0.056 mmol g^{-1} h^{-1} for TPE-Btz and 2.6 to 0.17 mmol g^{-1} h^{-1} in the case of TPE-Ttz (Figure 7e). This significant drop in H_2O_2 production in the presence of *p*-BQ suggests the major involvement of superoxide anion ($O_2^{\bullet-}$) intermediate during the H_2O_2 production, potentially via a two-step indirect $1e^-$ oxygen reduction reaction.[63,64] This is in line with the band potential diagram, where the higher CB potential of CMPs compared to the indirect ORR ($E^0_{O2/O2\cdot-}$ = −0.33 V vs NHE) enables an efficient electron transfer from CMP to oxygen at the catalyst surface. The $O_2^{\bullet-}$ subsequently reacts with a proton (H^+) to form a hydroperoxyl radical ($^{\bullet}OOH$) which then undergoes successive $1e^-/1H^+$ reduction yielding desired H_2O_2. The generation of $O_2^{\bullet-}$ was further confirmed and quantified by the oxidation of NBT dye (Figures S33–S35). Only a mere change in the H_2O_2 production was observed when isopropanol, IPA ($^{\bullet}OH$ scavenger) suggesting a minor contribution of $^{\bullet}OH$ species to the H_2O_2 formation (Figure 7e). Interestingly, upon introduction of EDTA (h^+ scavenger) caused a significant reduction in the H_2O_2 production, for instance, TPA-Btz produced only 0.221 mmol g^{-1} h^{-1} H_2O_2 when EDTA was introduced. This underlines the role of h^+ on the photocatalytic performance of the CMPs. Through both BA and EDTA being hole scavengers, BA showed significant enhancement in the H_2O_2 production, while the EDTA resulted in suppression. The enhancement in the presence of BA can be attributed to the following reasons: (i) upon oxidation by holes, BA forms α-hydroxybenzyl radical and releases protons. This increased proton concentration at the catalyst surface can enhance oxygen adsorption and the rate of oxygen reduction and consequently accelerate H_2O_2 generation via the superoxide anion pathway ($O_2 \rightarrow O_2^{\bullet-} \rightarrow OOH^* \rightarrow H_2O_2$). (ii) Moreover, the α-hydroxybenzyl radicals can act as reductants offering single electron transfer (SET) to the surface adsorbed oxygen, which simultaneously enhances the oxygen reduction and accelerates the H_2O_2 via the superoxide anion pathway. (iii) Upon oxidation by holes, benzyl alcohol forms benzaldehyde, which acts as a photosensitizer and, under light irradiation, forms α-hydroxybenzyl radicals, which in turn participate in the H_2O_2 production. Overall, in the presence of benzyl alcohol and photogenerated holes, an autocatalytic cycle is formed, significantly boosting H_2O_2 production rates.[61,65] On the other hand, EDTA, upon oxidation by holes, produces charged species that can bind to the catalyst surface via electrostatic interactions and inhibit proton and oxygen adsorption, thereby preventing oxygen reduction and H_2O_2 formation. Also, the large size of EDTA may block the pores of the CMP, hindering the oxygen diffusion to the bulk of the CMP catalyst, thereby reducing the H_2O_2 yields.[66] The scavenger experiments suggest that dominant formation of the superoxide anion ($O_2^{\bullet-}$) intermediate occurs during the H_2O_2 production. This was further confirmed by the electron paramagnetic resonance (EPR) spectroscopy. *In situ* EPR measurements on light-irradiated aqueous CMP dispersion added with 5,5-dimethyl-1-pyrroline N-oxide (DMPO) resulted in characteristic EPR signals corresponding to DMPO-OOH spin adduct, confirming the formation of $O_2^{\bullet-}$ intermediate during the H_2O_2 production (Figure 7f).[67] To elucidate the role of singlet oxygen ($^1O_2$) in photocatalytic H_2O_2 production, scavenger experiments were performed using L-histidine (L-His)[68] with TPA-Btz, TPE-Btz, and TPE-Ttz. A gradual decrease in H_2O_2 generation was observed upon L-His addition, indicating the involvement of $^1O_2$ (Figure S36). Further, the *in situ* EPR experiments using $^1O_2$ spin-trapping agent 2,2,6,6-tetramethyl-4-piperidone (TEMP) revealed strong EPR signals corresponding to TEMPO, confirming the involvement of $^1O_2$ in the photocatalytic process (Figure S37). Moreover, a characteristic near-infrared phosphorescence band at ∼1270 nm, corresponding to singlet oxygen, was observed in the presence of CMP photocatalysts (Figure S38), confirming the generation of $^1O_2$ during photocatalysis. Therefore, the above results indicated the involvement of $O_2^{\bullet-}$ and $^1O_2$ both in the H_2O_2 formation.

Computational Understanding of H_2O_2 Formation

Density functional theory (DFT) and time-dependent DFT (TD-DFT) calculations were performed on representative donor−acceptor (D−A) units to elucidate the relationship between the electronic structure and photocatalytic performance of the CMPs (TPA-Btz, TPE-Btz, and TPE-Ttz). The frontier molecular orbitals exhibit clear spatial separation, with the donor fragment predominantly contributing to the HOMO (shown by pink lobes) and the acceptor fragment primarily contributing to the LUMO (yellow lobes). As shown in Figure S39, in TPE-Btz, the HOMO is mainly localized on the phenyl-based donor, whereas the LUMO is concentrated on the acceptor unit. A similar distribution is observed in the other two systems, where the HOMO is largely delocalized over the donor (phenyl) moieties, and the LUMO is largely delocalized over the acceptor segments, indicating a comparable qualitative orbital localization across the series. Quantitatively, the calculated HOMO/LUMO energy levels are −5.44/−2.35 eV for TPA-Btz, −5.74/−2.35 eV for TPE-Btz, and −5.73/−2.34 eV for TPE-Ttz. The corresponding HOMO−LUMO gaps are 3.09, 3.39, and 3.39 eV, respectively. The relatively smaller gap of TPA-Btz suggests enhanced electronic reactivity and a greater propensity for intramolecular charge transfer, rationalizing its predicted superior photocatalytic activity among the three systems.

In the studied molecular systems, the primary atoms governing the electronic structure and chemical reactivity, such as C, N, O, and S, are *p*-block elements, with valence electrons predominantly occupying *p* orbitals. Consequently, the frontier electronic states responsible for optical excitation and photocatalytic activity are largely composed of *p*-orbital character. For this reason, the *p*-band gap provides a more direct and chemically meaningful measure of the energy difference between the valence and conduction states that actively participate in the excitation process. A smaller *p*-band gap thus indicates a lower excitation threshold within this relevant electronic subspace, which is closely associated with the enhanced photocatalytic potential. In contrast, the total density of states (TDOS) band gap incorporates contributions from all orbitals, including deeper-lying states that are not directly involved in optical transitions or subsequent reactive pathways. While the TDOS band gap provides a global

https://doi.org/10.1021/acsami.6c02471
ACS Appl. Mater. Interfaces XXXX, XXX, XXX−XXX

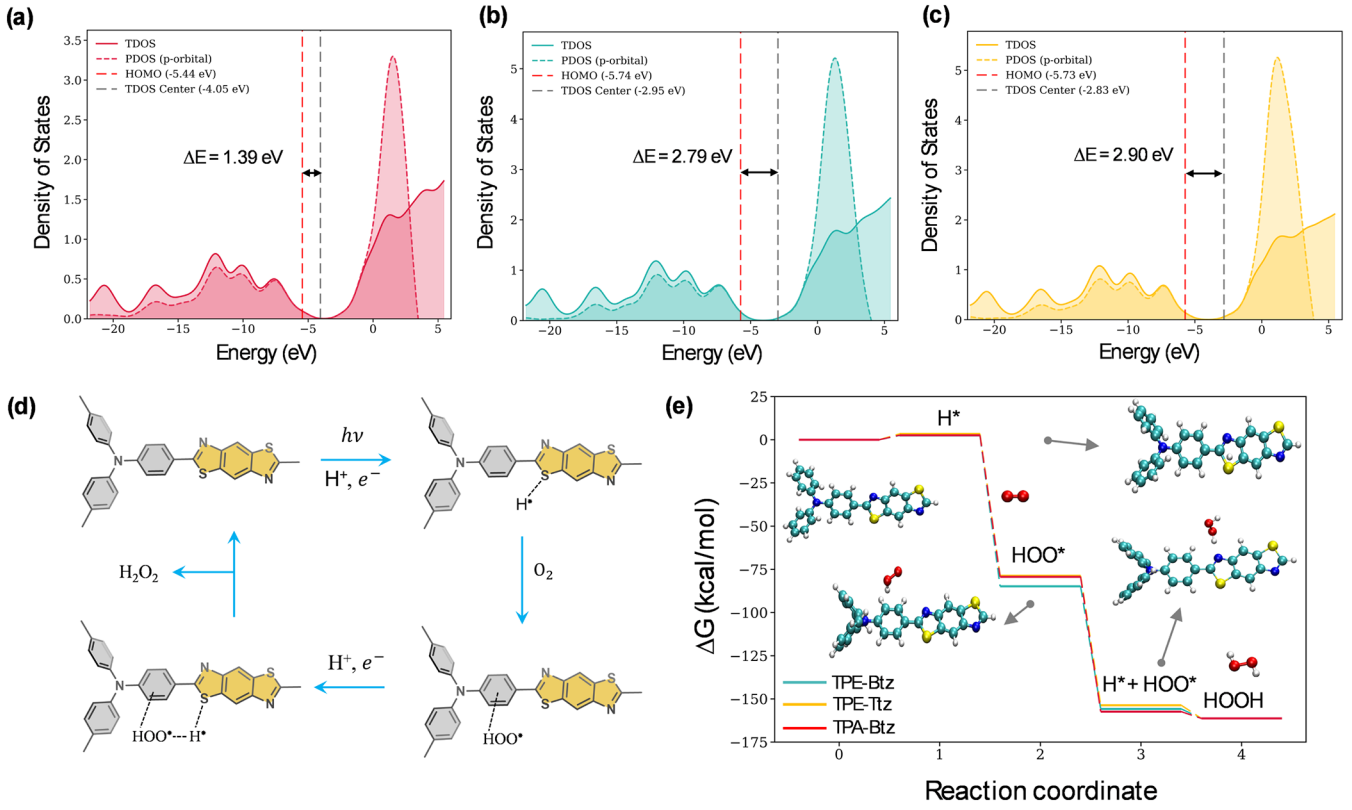

Figure 8. Computational analysis of H_2O_2 formation: total density of states (TDOS) for (a) TPA-Btz, (b) TPE-Btz, and (c) TPE-Ttz. (d) Photocatalytic H_2O_2 formation mechanism elucidated with the elementary unit of TPA-Btz. (e) Free energy profile of the oxygen reduction reaction pathway to H_2O_2 calculated for TPA-Btz, TPE-Btz, and TPE-Ttz. The corresponding DFT-optimized molecular fragments interacting with intermediates are shown in the ball-and-stick model in the inset.

description of the electronic structure, it does not selectively reflect the energetics of the orbitals that govern photocatalytic activity. Therefore, in the present context, the *p*-band gap serves as a more appropriate descriptor of the effective electronic transitions underlying the photocatalytic behavior in these systems. To obtain a comprehensive picture, both the total density of states (TDOS) and the projected density of states (PDOS) corresponding specifically to the *p*-orbitals were analyzed. The TDOS profiles represent the combined contribution of all participating orbitals, while the *p*-orbital PDOS highlights the specific contribution of the *p*-states. The TDOS (solid lines) and *p*-orbital PDOS (dashed lines) exhibit substantial overlap, demonstrating that the electronic states near the Fermi level are largely derived from *p*-orbitals. The HOMO levels and TDOS centers, indicated by vertical red and black lines, respectively, define the band gap, which serves as an indicator of orbital delocalization and charge transport efficiency; a smaller gap corresponds to higher reactivity, as shown in Figure S40. The corresponding p-band gap is shown in Figure 8a–c which is especially for the p-orbitals since p-orbitals are the participating orbitals in reaction, so their contribution is necessary. Among the investigated systems, TPA-Btz displays the narrowest *p*-band gap (ΔE = 1.39 eV; TDOS band gap = 1.39 eV), followed by TPE-Btz (ΔE = 1.51 eV; TDOS band gap = 2.79 eV) and TPE-Ttz (ΔE = 1.50 eV; TDOS band gap = 2.90 eV) (Figure 8a–c). These results confirm that TPA-Btz exhibits the most favorable charge-transfer characteristics and the highest efficiency for photocatalytic H_2O_2 generation. Based on thermodynamic analysis, a plausible photocatalytic mechanism for H_2O_2 generation over the CMP networks was established, highlighting a stepwise oxygen reduction reaction (ORR) pathway.[63] The Gibbs free energy (ΔG) profile indicates that the ORR proceeds through four elementary steps: (I) H adsorption (H*), (II) O_2 adsorption, (III) *OOH intermediate formation, and (IV) H_2O_2 generation, followed by desorption. In the first step, a proton (H^+) is adsorbed on the catalyst surface to form an adsorbed hydrogen species (H*). This process is essential for initiating the subsequent proton-coupled electron-transfer steps. The adsorbed hydrogen ensures the presence of an active hydrogen atom required for activating and reducing O_2 in the later stage. In step II, molecular oxygen binds to the preadsorbed hydrogen. Examination of the ΔG profile shows that the overall free-energy change between the initial and final states is negative for all three catalysts, confirming that the ORR is thermodynamically favorable. As expected for a state function, the overall ΔG remains unchanged across the catalysts; however, the individual elementary steps show catalyst-dependent variations. The first step (H* adsorption), which is photoinduced under UV activation, is mildly endergonic with a small positive ΔG (2–3 kcal/mol) for all systems. The subsequent O_2 adsorption step is strongly exergonic, with ΔG values of −81.93, −82.35, and −82.06 kcal/mol for TPA-Btz, TPE-Btz, and TPE-Ttz, respectively, showing minimal differences. The formation of the *OOH + H* intermediate is also exergonic, with ΔG values of −78.06, −70.98, and −74.96 kcal/mol for the same catalysts. This step is particularly significant, as the magnitude of the free-energy decrease varies notably among the CMPs. TPA-Btz exhibits the largest decrease in ΔG for *OOH + H* formation,

https://doi.org/10.1021/acsami.6c02471
ACS Appl. Mater. Interfaces XXXX, XXX, XXX−XXX

outperforming TPE-Btz and TPE-Ttz by 7.08 and 3.1 kcal/mol, respectively. Finally, H_2O_2 formation and desorption constitute an exergonic final step with ΔG values of −3.9, −5.5, and −7.65 kcal/mol (Figures 8d−e, S41, S42 and Table S3). Overall, these results demonstrate that *OOH + H* formation is the most energetically influential step in the ORR pathway and that TPA-Btz exhibits the most favorable thermodynamics for this step. Taken together, quantitative HOMO−LUMO analysis, TDOS/PDOS features, and the free-energy pathway all consistently support the conclusion that TPA-Btz is the most active photocatalyst, followed by TPE-Btz and TPE-Ttz, and support the experimental observations.

Preparation of Solid-Form H_2O_2

Commercial H_2O_2 is often available in liquid form and is associated with safety risks during transportation due to its low stability. This can be circumvented by formulating H_2O_2 into solid peroxides, such as sodium percarbonate ($Na_2CO_3 \cdot 1.5H_2O_2$). The solid form offers higher thermal stability, longer storage life, and reduced explosion hazard, and it enables controlled release. In view of this, the potential for producing a solid form of H_2O_2 was tested using the TPA-Btz catalyst. Upon addition of Na_2CO_3 to the filtrate of the reaction mixture generated after 1 h of light irradiation (which approximately produced 19.1 μM H_2O_2), a white solid precipitate was formed following the stoichiometric reaction eq 6.[69]

$$Na_2CO_3 + 1.5H_2O_2 \rightarrow Na_2CO_3 \cdot 1.5H_2O_2 \quad (6)$$

The formation of $Na_2CO_3 \cdot 1.5H_2O_2$ was confirmed by powder X-ray diffraction (PXRD) (Figure 7g). Furthermore, the FTIR spectrum of $Na_2CO_3 \cdot 1.5H_2O_2$ showed stretching frequencies of O−O (ν_{O-O}) and O−H (ν_{O-H}) at 885 and 3200−3400 cm^{-1}, respectively, confirming the formation of sodium percarbonate (Figure 7h). The activity of solid sodium percarbonate was demonstrated for the rapid degradation of organic pollutants such as methyl orange and methylene blue, highlighting its simplified use in environmental purification methods (Figure S43).

Recyclability

Recyclability and stability are key factors in assessing the commercial use of photocatalysts. It is well known that the strong C−C/C−N linkages present in CMPs offer high thermal and chemical stability. CMPs do not disintegrate even under harsh acidic or basic conditions, which are typical for polluted river water. Therefore, CMPs have high potential in commercial applications, especially for operating under harsh conditions. All the CMPs were tested for their recyclability in photocatalytic H_2O_2 production. As shown in Figure 7i, all the CMPs retained over ∼90% of their initial activity, highlighting their excellent recyclability. FTIR and TGA analyses were performed as evidence to confirm that the CMP networks remained stable after repeated use (Figures S44−S47), demonstrating their strong potential for long-term, real-world applications.

CONCLUSIONS

In summary, donor−acceptor CMPs demonstrate highly efficient visible-light-driven photocatalytic H_2O_2 production, achieving rates of up to 3.8 mmol g^{-1} h^{-1} in aqueous media and 54.7 mmol g^{-1} h^{-1} in an optimized biphasic system. Systematic modulation of D−A units enabled precise tuning of optical band gaps within 2.38−2.56 eV, thereby regulating light absorption; tunable exciton binding energies of ∼71−88 meV and charge generation at the surface. Time-resolved and steady-state Stern−Volmer quenching analysis revealed near-unity exciton-migration efficiency and rapid interfacial electron transfer kinetics at the CMP/solution interface. In-situ EPR analysis revealed the involvement of $^1O_2$ and competing $O_2^{\bullet-}$ pathway for H_2O_2 formation; hole-induced oxidation of $O_2^{\bullet-}$ to $^1O_2$ resulted in better charge carrier separation and accelerated kinetics of the ORR process; subsequently the H_2O_2 yields. DFT calculations corroborated the experimental observations of the ORR pathway for H_2O_2 formation. Collectively, these results elucidate the fundamental relationships among the molecular structure, exciton dynamics, and oxygen-reduction pathways in CMPs, offering clear design principles for efficient photocatalytic H_2O_2 production.

EXPERIMENTAL SECTION

Synthesis of TPA-Btz

A mixture of M1 (100 mg, 0.30 mmol, 1 equiv) and M2 (156.91 mg, 0.91 mmol, 3 equiv) was placed in a J. Young cylindrical Schlenk tube, and 4 mL of DMAc was added. The suspension was sonicated and then degassed by three freeze−pump−thaw cycles before being heated in an oven at 150 °C for 96 h. The resulting solids were collected by filtration, washed thoroughly with CH_2Cl_2, and further purified by Soxhlet extraction with CH_2Cl_2, methanol, and THF for 6 h each. The pure product, TPA-Btz, was obtained as a pale yellow solid (Yield: 88.5%).

Synthesis of TPE-Btz

A mixture of M3 (100 mg, 0.13 mmol, 1 equiv) and M2 (46.04 mg, 0.26 mmol, 2 equiv) was placed in a J. Young cylindrical Schlenk tube, and 4 mL of DMAc was added. The resulting suspension was sonicated and subjected to three freeze−pump−thaw cycles before being heated in an oven at 150 °C for 96 h. The obtained solids were collected by filtration, washed with CH_2Cl_2, and further purified by Soxhlet extraction with CH_2Cl_2, methanol, and THF for 6 h each to obtain pure TPE-Btz as a pale yellow solid (Yield: 82%).

Synthesis of lpTPE-Btz

A mixture of monomer M5 (150 mg, 0.27 mmol, 1 equiv) and M2 (48 mg, 0.27 mmol, 1 equiv) was placed in a J. Young cylindrical Schlenk tube, and 4 mL of DMAc was added. The suspension was sonicated, degassed via three freeze−pump−thaw cycles, and heated at 150 °C for 96 h. The resulting pale-yellow solid was separated by filtration, washed, and purified via Soxhlet extraction with CH_2Cl_2, methanol, and THF for 6 h each to yield the pure product, lpTPE-Btz (Yield: 80%).

ASSOCIATED CONTENT

Supporting Information

The Supporting Information is available free of charge at https://pubs.acs.org/doi/10.1021/acsami.6c02471.

Additional experimental details, synthetic procedures, photocatalytic setup, material characterization data (FTIR, TGA, BET, morphology: TEM and EDS mapping, photophysical data (optical properties, quenching analysis), AQY, kinetics, calibration and scavenging, and DFT calculations (PDF)

AUTHOR INFORMATION

Corresponding Authors

Venkata Suresh Mothika − *Department of Chemistry, Indian Institute of Technology (IIT) Kanpur, Kalyanpur, Uttar*

https://doi.org/10.1021/acsami.6c02471
ACS Appl. Mater. Interfaces XXXX, XXX, XXX−XXX

Pradesh 208016, India; orcid.org/0000-0002-3084-1279; Email: smothika@iitk.ac.in

Anirban Mondal – *Department of Chemistry, Indian Institute of Technology (IIT) Gandhinagar, Palaj, Gujarat 382055, India;* orcid.org/0000-0003-3029-8840; Email: amondal@iitgn.ac.in

Authors

Atul Kapoor – *Department of Chemistry, Indian Institute of Technology (IIT) Kanpur, Kalyanpur, Uttar Pradesh 208016, India*

Laraib Akhtar – *Department of Chemistry, Indian Institute of Technology (IIT) Kanpur, Kalyanpur, Uttar Pradesh 208016, India*

Sanyam – *Department of Chemistry, Indian Institute of Technology (IIT) Gandhinagar, Palaj, Gujarat 382055, India;* orcid.org/0000-0001-7410-8207

Suman Karmakar – *Department of Chemistry, Indian Institute of Technology (IIT) Kharagpur, Kharagpur, West Bengal 721302, India;* orcid.org/0009-0009-6293-8524

Complete contact information is available at: https://pubs.acs.org/10.1021/acsami.6c02471

Author Contributions

A.K. and L.A.: investigation, methodology, formal analysis, data curation, validation, writing of the original draft. Sanyam: DFT investigation, data curation, methodology, draft editing. S.K.: EPR investigation. A.M.: DFT methodology, formal analysis, draft editing. V.S.M.: conceptualization, funding acquisition, project administration, supervision, writing of the original draft, review, and editing. All authors have read and approved the manuscript. A.K. and L.A. contributed equally to this work.

Notes

The authors declare no competing financial interest.

■ ACKNOWLEDGMENTS

A.K. thanks IIT Kanpur for the Institute Postdoc fellowship. LY acknowledges UGC, India, for the PhD research fellowship. VSM acknowledges financial support from IITK (Grant No: IITK/CHM/2022233) and the Anusandhan National Research Foundation (ANRF, Grant No. SRG/2023/000062), India. The authors thank IITK for its infrastructure and analytical facilities. The authors thank Dr. Suman Kalyan Samanta for fruitful discussions. The authors thank Dr. Soumyabrata Roy and Juhina Nisar for BET measurements.

■ REFERENCES

(1) Freese, T.; Meijer, J. T.; Brands, M. B.; Alachouzos, G.; Stuart, M. C. A.; Tarozo, R.; Gerlach, D.; Smits, J.; Rudolf, P.; Reek, J. N. H.; Feringa, B. L. Iron Oxide-Promoted Photochemical Oxygen Reduction to Hydrogen Peroxide (H_2O_2). *EES Catal.* **2024**, *2* (1), 262–275.

(2) Freese, T.; Matei, A.; Brands, M. B.; Karsakova, M.; Acevedo–Guzmán, D. A.; Gerlach, D.; Rudolf, P.; Reek, J. N. H.; Feringa, B. L. Precious Metal-Free Artificial Leaf for Photosynthesis of Hydrogen Peroxide from Water. *ChemSusChem* **2025**, *18* (21), No. e202501055.

(3) Yao, L.; Pütz, A. M.; Vignolo-González, H.; Lotsch, B. V. Covalent Organic Frameworks as Single-Site Photocatalysts for Solar-to-Fuel Conversion. *J. Am. Chem. Soc.* **2024**, *146* (14), 9479–9492.

(4) Freese, T.; Meijer, J. T.; Miola, M.; Pescarmona, P. P.; Feringa, B. L. Photochemical On-Demand Production of Hydrogen Peroxide in a Modular Flow Reactor. *Sustainable Energy Fuels* **2024**, *9* (1), 141–151.

(5) Peduru Hewa, T. M.; Tannock, G. A.; Mainwaring, D. E.; Harrison, S.; Fecondo, J. V. The Detection of Influenza A and B Viruses in Clinical Specimens Using a Quartz Crystal Microbalance. *J. Virol. Methods* **2009**, *162* (1), 14–21.

(6) Wang, S.; Xie, Z.; Zhu, D.; Fu, S.; Wu, Y.; Yu, H.; Lu, C.; Zhou, P.; Bonn, M.; Wang, H. I.; et al. Efficient Photocatalytic Production of Hydrogen Peroxide Using Dispersible and Photoactive Porous Polymers. *Nat. Commun.* **2023**, *14* (1), 6891.

(7) Xu, Y.; Jin, S.; Xu, H.; Nagai, A.; Jiang, D. Conjugated Microporous Polymers: Design, Synthesis and Application. *Chem. Soc. Rev.* **2013**, *42* (20), 8012–8031.

(8) Kapoor, A.; Sahoo, N.; Rajput, S. K.; Samanta, P. K.; Mothika, V. S. Dual Function: Practical Nanomolar Antibiotic Detection and Photocatalytic Micropollutant Degradation Using Thiazolothiazole-Conjugated Microporous Polymers. *ACS Appl. Polym. Mater.* **2025**, *7* (11), 7672–7685.

(9) Rajput, S. K.; Mothika, V. S. Powders to Thin Films: Advances in Conjugated Microporous Polymer Chemical Sensors. *Macromol. Rapid Commun.* **2024**, *45* (10), 2300730.

(10) Chen, J.; Yan, W.; Townsend, E. J.; Feng, J.; Pan, L.; Del Angel Hernandez, V.; Faul, C. F. J. Tunable Surface Area, Porosity, and Function in Conjugated Microporous Polymers. *Angew. Chem., Int. Ed.* **2019**, *58* (34), 11715–11719.

(11) Mothika, V. S.; Sutar, P.; Verma, P.; Das, S.; Pati, S. K.; Maji, T. K. Regulating Charge-Transfer in Conjugated Microporous Polymers for Photocatalytic Hydrogen Evolution. *Chem. - Eur. J.* **2019**, *25* (15), 3867–3874.

(12) Liao, Y.; Zeng, J.; Kang, S.; Wu, Q.; Cui, H.; Zhang, W.; Yi, B.; Liu, C.; Yang, H. Strengthening Hydrogen Bonds of Clay/Conjugated Microporous Polymer Composites for Advancing Visible-Light-Driven Antibiotic Removal. *Sep. Purif. Technol.* **2026**, *387*, 136589.

(13) Song, W.; Zhang, Y.; Tran, C. H.; Choi, H. K.; Yu, D.-G.; Kim, I. Porous Organic Polymers with Defined Morphologies: Synthesis, Assembly, and Emerging Applications. *Prog. Polym. Sci.* **2023**, *142*, 101691.

(14) Yang, K.; Chen, L.; Xiong, K.; Yang, J.; Adeli, M.; Li, S.; Wang, M.; Cheng, C.; Zhao, C. Bisite Sulfonate-Functionalized Covalent Organic Frameworks with Efficient and Dynamic Proton Transportation for Accelerating H_2O_2 Photosynthesis. *Adv. Funct. Mater.* **2026**, *36* (15), No. e20900.

(15) Deng, X.; Xiang, R.; Liu, M.; Yi, B.; Zhang, W.; Liu, C.; Yang, H. Molecular Oxygen Activation Mediated by Exciton Effects in CMPs@Sepiolite for Photocatalytic Elimination of Emerging Contaminants. *Chem. Eng. J.* **2026**, *527*, 171570.

(16) Wu, S.; Quan, X. Design Principles and Strategies of Photocatalytic H_2O_2 Production from O_2 Reduction. *ACS ES&T Eng.* **2022**, *2* (6), 1068–1079.

(17) Zhang, H.; Wei, W.; Chi, K.; Zheng, Y.; Kong, X. Y.; Ye, L.; Zhao, Y.; Zhang, K. A. I. Enhanced Photocatalytic Production of Hydrogen Peroxide by Covalent Triazine Frameworks with Stepwise Electron Transfer. *ACS Catal.* **2024**, *14* (23), 17654–17663.

(18) Zhou, S.; Zhu, Q.; Kan, L.; Xu, H.; Luo, X.; Zhu, L.; Wang, D.; Liu, G.; Gu, P. Achieving a Simultaneous Charge- and Energy-Involved Dual-Channel Mechanism in Spirobifluorene-Based Conjugated Organic Polymers for Enhanced H_2O_2 Photosynthesis. *J. Am. Chem. Soc.* **2025**, *147* (48), 44492–44506.

(19) Ma, B. C.; Ghasimi, S.; Landfester, K.; Zhang, K. A. I. Enhanced Visible Light Promoted Antibacterial Efficiency of Conjugated Microporous Polymer Nanoparticles via Molecular Doping. *J. Mater. Chem. B* **2016**, *4* (30), 5112–5118.

(20) Xue, Q.; Li, H.; Jin, P.; Zhou, X.; Wang, F. Singlet-Oxygen-Driven Cooperative Photocatalytic Coupling of Biomass Valorization and Hydrogen Peroxide Production Using Covalent Organic Frameworks. *Angew. Chem., Int. Ed.* **2025**, *64* (19), No. e202423368.

(21) Liu, X.; Qi, R.; Li, S.; Liu, W.; Yu, Y.; Wang, J.; Wu, S.; Ding, K.; Yu, Y. Triazine–Porphyrin-Based Hyperconjugated Covalent Organic Framework for High-Performance Photocatalysis. *J. Am. Chem. Soc.* **2022**, *144* (51), 23396–23404.

(22) Cheng, J.; Wan, S.; Cao, S. Promoting Solar-Driven Hydrogen Peroxide Production over Thiazole-Based Conjugated Polymers via Generating and Converting Singlet Oxygen. *Angew. Chem., Int. Ed.* **2023**, *62* (40), No. e202310476.
(23) Chakraborty, A.; Chakrabortty, P.; Pachfule, P. Covalent Organic Framework for Photocatalytic Hydrogen Peroxide Production: A Green Pathway. *Chem. Mater.* **2025**, *37* (24), 9614−9632.
(24) Mi, X.; Li, J.; Lyu, W.; Xu, L.; Liu, Y.; Qian, C.; Yu, J.; He, W.; Feng, J.; Liao, Y. Boosting Fenton-like Reaction via Enhanced Charge Transfer in Donor-Acceptor Polyaniline-like Conjugated Microporous Polymers. *Appl. Catal. B Environ. Energy* **2025**, *378*, 125530.
(25) Buglak, A. A.; Charisiadis, A.; Sheehan, A.; Kingsbury, C. J.; Senge, M. O.; Filatov, M. A. Quantitative Structure-Property Relationship Modelling for the Prediction of Singlet Oxygen Generation by Heavy-Atom-Free BODIPY Photosensitizers. *Chem. - Eur. J.* **2021**, *27* (38), 9934−9947.
(26) He, L.; Dong, J.; Yang, Y.; Huang, Z.; Ye, S.; Ke, X.; Zhou, Y.; Li, A.; Zhang, Z.; Wu, S.; Wang, Y.; Cai, S.; Liu, X.; He, Y. Accelerating the Discovery of Type II Photosensitizer: Experimentally Validated Machine Learning Models for Predicting the Singlet Oxygen Quantum Yield of Photosensitive Molecule. *J. Mol. Struct.* **2025**, *1321*, 139850.
(27) Ksenofontov, A. A.; Eremeeva, Y. V.; Bocharov, P. S.; Makarov, D. M. SpecML: Web Tool for Predicting the Spectral Properties of BODIPYs. *Spectrochim. Acta, Part A* **2026**, *348*, 127091.
(28) Qin, C.; Wu, X.; Tang, L.; Chen, X.; Li, M.; Mou, Y.; Su, B.; Wang, S.; Feng, C.; Liu, J.; et al. Dual Donor-Acceptor Covalent Organic Frameworks for Hydrogen Peroxide Photosynthesis. *Nat. Commun.* **2023**, *14* (1), 5238.
(29) Biswal, B. P.; Vignolo-González, H. A.; Banerjee, T.; Grunenberg, L.; Savasci, G.; Gottschling, K.; Nuss, J.; Ochsenfeld, C.; Lotsch, B. V. Sustained Solar H_2 Evolution from a Thiazolo[5,4-d]Thiazole-Bridged Covalent Organic Framework and Nickel-Thiolate Cluster in Water. *J. Am. Chem. Soc.* **2019**, *141* (28), 11082−11092.
(30) Sau, S.; Samanta, S. K. Triphenylamine−Anthraquinone Based Donor−Acceptor Conjugated Microporous Polymers for Photocatalytic Hydroxylation of Phenylboronic Acids. *Chem. Commun.* **2023**, *59* (5), 635−638.
(31) Wang, R.; Zhou, H.; Fang, Q.; Su, Z.; Qiu, S. Recent Advances in Covalent Organic Framework-Based Catalysts for the Electrosynthesis of Hydrogen Peroxide. *Chem. Commun.* **2025**, *61* (79), 15346−15361.
(32) Lee, J.-S. M.; Cooper, A. I. Advances in Conjugated Microporous Polymers. *Chem. Rev.* **2020**, *120* (4), 2171−2214.
(33) Liu, L.; Gao, M.-Y.; Yang, H.; Wang, X.; Li, X.; Cooper, A. I. Linear Conjugated Polymers for Solar-Driven Hydrogen Peroxide Production: The Importance of Catalyst Stability. *J. Am. Chem. Soc.* **2021**, *143* (46), 19287−19293.
(34) Saka, E.; Bıyıklıoğlu, Z.; Kantekin, H. Microwave-Assisted Synthesis and Characterization of Co(II) Phthalocyanine and Investigation of Its Catalytic Activity on 4-Nitrophenol Oxidation. *Turk. J. Chem.* **2014**, *38*, 1166−1173.
(35) Wang, H.; Thangamuthu, M.; Wu, Z.; Yang, J.; Yuan, H.; Bayazit, M. K.; Tang, J. Self-Assembled Sulphur Doped Carbon Nitride for Photocatalytic Water Reforming of Methanol. *Chem. Eng. J.* **2022**, *445*, 136790.
(36) Kao, Y.-C.; Mohamed, M. G.; Chen, Y.-H.; Ejaz, M.; Kuo, S.-W. Synergistic Engineering of Pyrene−Thiazolothiazole-Based Donor−π−Acceptor Conjugated Microporous Polymers with Heteroatom Embedding for Efficient Visible-Light Photocatalyst for Organic Dye Degradation. *ACS Polym. Au.* **2025**, *5* (5), 633−644.
(37) Barawi, M.; Collado, L.; Gomez-Mendoza, M.; Oropeza, F. E.; Liras, M.; de la Peña O'Shea, V. A. Conjugated Porous Polymers: Ground-Breaking Materials for Solar Energy Conversion. *Adv. Energy Mater.* **2021**, *11* (43), 2101530.
(38) Molina, A.; Patil, N.; Ventosa, E.; Liras, M.; Palma, J.; Marcilla, R. New Anthraquinone-Based Conjugated Microporous Polymer Cathode with Ultrahigh Specific Surface Area for High-Performance Lithium-Ion Batteries. *Adv. Funct. Mater.* **2020**, *30* (6), 1908074.
(39) Lu, F.; Che, Y.; Tian, H.; Cai, Y.; Kong, Q.; Yao, X.; Su, Z. Anthraquinone-Based Conjugated Microporous Polymer as Anode for Long-Life Lithium Batteries. *ACS Appl. Polym. Mater.* **2024**, *6* (24), 15114−15123.
(40) Cheng, Z.; He, Y.; Yang, C.; Meng, N.; Liao, Y. Metal-Free Synthesis of Pyridyl Conjugated Microporous Polymers with Tunable Bandgaps for Efficient Visible-Light-Driven Hydrogen Evolution. *Chin. Chem. Lett.* **2023**, *34* (4), 107440.
(41) Xu, Y.; Nagai, A.; Jiang, D. Core−Shell Conjugated Microporous Polymers: A New Strategy for Exploring Color-Tunable and -Controllable Light Emissions. *Chem. Commun.* **2013**, *49* (16), 1591−1593.
(42) Chen, L.; Honsho, Y.; Seki, S.; Jiang, D. Light-Harvesting Conjugated Microporous Polymers: Rapid and Highly Efficient Flow of Light Energy with a Porous Polyphenylene Framework as Antenna. *J. Am. Chem. Soc.* **2010**, *132* (19), 6742−6748.
(43) Kent, C. A.; Liu, D.; Ma, L.; Papanikolas, J. M.; Meyer, T. J.; Lin, W. Light Harvesting in Microscale Metal−Organic Frameworks by Energy Migration and Interfacial Electron Transfer Quenching. *J. Am. Chem. Soc.* **2011**, *133* (33), 12940−12943.
(44) Zeng, X.; Wang, T.; Wang, Z.; Tebyetekerwa, M.; Liu, Y.; Liu, Z.; Wang, G.; Wibowo, A. A.; Pierens, G.; Gu, Q.; Zhang, X. Fast Photocatalytic Hydrogen Peroxide Generation by Singlet Oxygen-Engaged Sequential Excitation Energy and Electron-Transfer Process. *ACS Catal.* **2024**, *14* (13), 9955−9968.
(45) Choi, S.; Jung, W.-J.; Park, K.; Kim, S.-Y.; Baeg, J.-O.; Kim, C. H.; Son, H.-J.; Pac, C.; Kang, S. O. Rapid Exciton Migration and Amplified Funneling Effects of Multi-Porphyrin Arrays in a Re(I)/Porphyrinic MOF Hybrid for Photocatalytic CO_2 Reduction. *ACS Appl. Mater. Interfaces* **2021**, *13* (2), 2710−2722.
(46) Deshmukh, A.; Bandyopadhyay, S.; James, A.; Patra, A. Trace Level Detection of Nitroanilines Using a Solution Processable Fluorescent Porous Organic Polymer. *J. Mater. Chem. C* **2016**, *4* (20), 4427−4433.
(47) Lehrer, S. S. Solute Perturbation of Protein Fluorescence. The Quenching of the Tryptophyl Fluorescence of Model Compounds and of Lysozyme by Iodide Ion. *Biochemistry* **1971**, *10* (17), 3254−3263.
(48) Cao, L.; Lin, Z.; Shi, W.; Wang, Z.; Zhang, C.; Hu, X.; Wang, C.; Lin, W. Exciton Migration and Amplified Quenching on Two-Dimensional Metal−Organic Layers. *J. Am. Chem. Soc.* **2017**, *139* (20), 7020−7029.
(49) Muhammad, Z.; Rashid, A. Exciton Binding Energies and Polaron Interplay in the Optically Excited State of Organic−Inorganic Lead Halide Perovskites. *Mater. Adv.* **2025**, *6* (1), 13−38.
(50) Sugie, A.; Nakano, K.; Tajima, K.; Osaka, I.; Yoshida, H. Dependence of Exciton Binding Energy on Bandgap of Organic Semiconductors. *J. Phys. Chem. Lett.* **2023**, *14* (50), 11412−11420.
(51) Bai, Y.; Wilbraham, L.; Slater, B. J.; Zwijnenburg, M. A.; Sprick, R. S.; Cooper, A. I. Accelerated Discovery of Organic Polymer Photocatalysts for Hydrogen Evolution from Water through the Integration of Experiment and Theory. *J. Am. Chem. Soc.* **2019**, *141* (22), 9063−9071.
(52) Wang, K.; Shen, Z.; Qi, F.; Yuan, Y.; Xiao, C.; Pan, H. Recent Advances in Built-in Electric Field for Efficient Energy Electrocatalysis. *Carbon Neutralization* **2025**, *4* (5), No. e70029.
(53) Chen, W.; Kan, L.; Luo, X.; Wang, D.; Zhu, L.; Liu, G.; Liu, P.; Zhou, S.; Gu, P.; Zhang, G. Balance and Optimization of Oxygen Reduction Reaction Pathways on Hydroxyl-Containing Conjugated Microporous Polymers for Improved Hydrogen Peroxide Photogeneration. *Adv. Funct. Mater.* **2026**, No. e74461.
(54) Arabacı, B.; Bakır, R.; Orak, C.; Yüksel, A. Predictive Modeling of Photocatalytic Hydrogen Production: Integrating Experimental Insights with Machine Learning on Fe/g-C3N4 Catalysts. *Ind. Eng. Chem. Res.* **2025**, *64* (10), 5184−5199.
(55) Zhang, W.; Sun, M.; Cheng, J.; Wu, X.; Xu, H. Regulating Electron Distribution in Regioisomeric Covalent Organic Frameworks

https://doi.org/10.1021/acsami.6c02471
ACS Appl. Mater. Interfaces XXXX, XXX, XXX−XXX

for Efficient Solar-Driven Hydrogen Peroxide Production. *Adv. Mater.* **2025**, *37* (18), 2500913.
(56) Zhao, Y.; Ge, H.; Kondo, Y.; Guo, Z.; Kuwahara, Y.; Mori, K.; Sekino, T.; Bian, Z.; Yamashita, H. Highly Reactive Facet Modulation of Ti-Based MOFs by Selective Anchoring of Au Metal for Photocatalytic H_2O_2 Production. *ACS Catal.* **2025**, *15* (13), 11313−11325.
(57) Luo, X.; Zhang, Y.; Zhou, S.; Wang, P.; Wang, D.; Gu, P. A Near-Infrared-II Light-Response BODIPY-Based Conjugated Microporous Polymer for Enhanced Photocatalytic Degradation of Cationic Dyes and H_2O_2 Production. *Chem. Commun.* **2024**, *60* (61), 7910−7913.
(58) Duan, J.; Teng, L.; Liu, H.; Zhang, X.; Yu, H.; Huang, Q.; Li, Y.; Liu, M.; Hu, H.; Lyu, W.; et al. Heteroporous Donor-Acceptor Covalent Organic Framework Cathode for High-Rate-Capacity Lithium-Ion Battery. *Angew. Chem., Int. Ed.* **2025**, *64* (42), No. e202517853.
(59) Duan, J.; Chen, F.; Yu, H.; Zhu, S.; Teng, L.; Wang, K.; Chen, T.; Lyu, W.; Hu, H.; Liao, Y. π-Bridge-Linked Ionic Covalent Organic Framework with Fast Reaction Kinetics for High-Rate-Capacity Lithium-Ion Batteries. *Angew. Chem.* **2025**, *137* (30), No. e202505207.
(60) Chakraborty, A.; Alam, A.; Pal, U.; Sinha, A.; Das, S.; Saha-Dasgupta, T.; Pachfule, P. Enhancing Photocatalytic Hydrogen Peroxide Generation by Tuning Hydrazone Linkage Density in Covalent Organic Frameworks. *Nat. Commun.* **2025**, *16* (1), 503.
(61) Xu, Z.; Fang, W.; Zhou, F.; Jiang, C.; Zheng, J.; Li, Y.; Zhang, S.; Bao, Z.; Cao, Q.; Wang, J. Synergistic Photocatalytic Synthesis of H_2O_2: Mechanistic Insights and Sustainable Applications. *AIChE J.* **2025**, *71* (3), No. e18692.
(62) Chen, N.; Fang, G.; Liu, G.; Zhou, D.; Gao, J.; Gu, C. The Effects of Fe-Bearing Smectite Clays on OH Formation and Diethyl Phthalate Degradation with Polyphenols and H_2O_2. *J. Hazard. Mater.* **2018**, *357*, 483−490.
(63) Yang, T.; Zhang, D.; Kong, A.; Zou, Y.; Yuan, L.; Liu, C.; Luo, S.; Wei, G.; Yu, C. Robust Covalent Organic Framework Photocatalysts for H_2O_2 Production: Linkage Position Matters. *Angew. Chem., Int. Ed.* **2024**, *63* (22), No. e202404077.
(64) Wu, W.; Li, Z.; Liu, S.; Zhang, D.; Cai, B.; Liang, Y.; Wu, M.; Liao, Y.; Zhao, X. Pyridine-Based Covalent Organic Frameworks with Pyridyl-Imine Structures for Boosting Photocatalytic H_2O_2 Production via One-Step 2e− Oxygen Reduction. *Angew. Chem., Int. Ed.* **2024**, *63* (23), No. e202404563.
(65) Katsamitros, A.; Giannakakis, A. N.; Karamoschos, N.; Karousis, N.; Tasis, D. Covalent Organic Frameworks for Photocatalytic Hydrogen Peroxide Evolution. *Chem. - Eur. J.* **2025**, *31* (15), No. e202404272.
(66) Shah, B. R.; Patel, U. D. Mechanistic Aspects of Photocatalytic Degradation of Lindane by TiO_2 in the Presence of Oxalic Acid and EDTA as Hole-Scavengers. *J. Environ. Chem. Eng.* **2021**, *9* (4), 105458.
(67) Clément, J.-L.; Ferré, N.; Siri, D.; Karoui, H.; Rockenbauer, A.; Tordo, P. Assignment of the EPR Spectrum of 5,5-Dimethyl-1-Pyrroline N-Oxide (DMPO) Superoxide Spin Adduct. *J. Org. Chem.* **2005**, *70* (4), 1198−1203.
(68) Zhao, S.; Zhao, X. Insights into the Role of Singlet Oxygen in the Photocatalytic Hydrogen Peroxide Production over Polyoxometalates-Derived Metal Oxides Incorporated into Graphitic Carbon Nitride Framework. *Appl. Catal., B* **2019**, *250*, 408−418.
(69) Yue, J.-Y.; Xu, Z.-S.; Luo, J.-X.; Yang, P.; Tang, B. Architecting Covalent Organic Frameworks across Dimensions for Efficient H_2O_2 Photoproduction. *ACS Catal.* **2025**, *15* (14), 12541−12550.

https://doi.org/10.1021/acsami.6c02471
ACS Appl. Mater. Interfaces XXXX, XXX, XXX−XXX